

A Level Set Method on Particle Flow Maps

Jinjin He^{a,*}, Taiyuan Zhang^b, Zhiqi Li^a, Junwei Zhou^c, Duowen Chen^a, Bo Zhu^a

^a*School of Interactive Computing, Georgia Institute of Technology, Atlanta, 30332, Georgia, USA*

^b*Department of Computer Science, Dartmouth College, Hanover, 03755, New Hampshire, USA*

^c*Computer Science and Engineering, University of Michigan, Ann Arbor, 48109, Michigan, USA*

Abstract

This paper introduces a Particle Flow Map Level Set (PFM-LS) method for high-fidelity interface tracking. We store level-set values, gradients, and Hessians on particles concentrated in a narrow band around the interface, advecting them via bidirectional flow maps while using a conventional grid-based representation elsewhere. By interpreting the level set value as a 3-form and its gradient as a 1-form, PFM-LS achieves exceptional geometric fidelity during complex deformations and preserves sub-grid features that traditional methods cannot capture. Our dual-timescale approach utilizes long-range maps for values and gradients, with frequent reinitialization of short-range maps for the distortion-sensitive Hessian, alongside adaptive particle control that maintains sufficient density within the narrow band. We also develop a hybrid particle-grid quasi-Newton redistancing scheme that preserves fine-scale features while enforcing the signed-distance property. Benchmark comparisons in 2D and 3D demonstrate that PFM-LS achieves state-of-the-art volume preservation and shape fidelity against a broad range of existing level-set methods.

Keywords: Level Set, Particle Level Set, Characteristic Mapping, Particle Flow Map, Interface Tracking

1. Introduction

The level set method, introduced by Osher and Sethian [45, 50, 43], represents interfaces implicitly as the zero isocontour of a signed distance function and has since become a foundational tool for interface tracking in free-surface simulations [59, 3,

*Corresponding author.

¹E-mail addresses: jhe433@gatech.edu (Jinjin He), imaginer.tai@gmail.com (Taiyuan Zhang), zli3167@gatech.edu (Zhiqi Li), zjw330501@gmail.com (Junwei Zhou), dchen322@gatech.edu (Duowen Chen), bo.zhu@gatech.edu (Bo Zhu).

28, 13, 8, 60], multiphase flows [58, 37, 52, 53, 55, 64], and other interface-driven dynamics [44, 17, 18, 10, 7, 20]. The central idea of the level set method is to represent an interface $\partial\Omega$ implicitly as the zero isocontour of a signed distance function $\varphi(\mathbf{x}, t)$:

$$\partial\Omega(t) = \{\mathbf{x} \in \mathbb{R}^d : \varphi(\mathbf{x}, t) = 0\}, \quad (1)$$

where $\varphi > 0$ in the air domain Ω_0 and $\varphi < 0$ in the liquid domain Ω_1 . The evolution of the interface under a velocity field $\mathbf{u}(\mathbf{x}, t)$ is governed by the level set advection equation:

$$\frac{\partial \varphi}{\partial t} + \mathbf{u} \cdot \nabla \varphi = 0. \quad (2)$$

This implicit representation naturally accommodates complex topological changes such as merging and splitting without explicit remeshing [1, 47, 49], making level set methods indispensable for a wide range of computational physics applications [44, 51, 17, 18]. Despite their versatility, classical level set methods suffer from two fundamental limitations when solving Eq. (2) numerically. First, numerical diffusion during advection causes substantial volume loss, particularly for thin structures and small-scale features undergoing large deformation [12, 15, 8]. Even with high-order spatial discretizations such as ENO [54] or WENO [36, 25] schemes, the repeated interpolation and reinitialization steps introduce cumulative errors that erode interface fidelity over time. Second, the discrete grid representation lacks the resolution to capture sub-grid geometric details, leading to the gradual erosion of sharp corners and filaments that are crucial for visual and physical fidelity [21, 53].

Particle Level Set. These limitations motivate the development of numerical methods assisted by Lagrangian structures that can better preserve interface geometry over long time horizons. The hybrid particle level set (PLS) method [12] employs marker particles distributed near the interface within a narrow band to correct the signed distance function φ . Each particle p carries its own signed distance value φ_p and is advected along the flow:

$$\frac{d\mathbf{x}_p}{dt} = \mathbf{u}(\mathbf{x}_p, t). \quad (3)$$

When discrepancies arise between the particle values φ_p and the grid values $\varphi(\mathbf{x}_p)$, the particles provide correction information to reduce volume loss and maintain sharper interfaces [46, 22, 23, 29, 38, 16]. Subsequent extensions have further improved accuracy and robustness: for instance, oriented and gradient-augmented variants [65, 16] embed additional geometric information such as the interface normal $\mathbf{n} = \nabla\varphi/|\nabla\varphi|$ or gradient $\mathbf{g} = \nabla\varphi$ within particles to better preserve curvature and local detail. In addition, the one-layer PLS formulation [23, 65, 73, 74] simplifies particle management by confining particles to a single layer near the interface

without compromising reinitialization accuracy. More recently, diffusion-driven characteristic mapping [69] has enhanced particle redistribution by maintaining uniform and stable marker distributions during large deformations, and neural extensions [7] leverage learned corrections for adaptive and data-driven interface tracking.

Despite these advances, existing particle-based level set methods still face fundamental limitations in long-range advection. First, the level set function φ on the grid is advected using conventional schemes (e.g., semi-Lagrangian), which introduces numerical dissipation that particles can only partially correct. Second, periodic particle reseeding necessary to maintain adequate particle coverage discards old particles and initializes new ones by interpolating φ from the current grid, thereby introducing additional errors and erasing the trajectory history carried by the original particles. Most critically, particles in these methods store only their current position \mathbf{x}_p and level set value φ_p , without retaining their initial positions \mathbf{X}_p . As a result, the natural flow map encoded by particle trajectories is never exploited, and the long-range characteristic structure of the advection equation remains unutilized.

Gradient Augmented Level Set. Complementary grid-based strategies have also been developed to improve advection accuracy and volume preservation. Among these, gradient-augmented level set (GALS) methods [42] are most closely related to the present work. GALS methods extend the formulation by evolving both the level set φ and its gradient $\mathbf{g} = \nabla\varphi$ as independent variables, satisfying

$$\frac{\partial \mathbf{g}}{\partial t} + (\mathbf{u} \cdot \nabla) \mathbf{g} + (\nabla \mathbf{u})^\top \mathbf{g} = 0, \quad (4)$$

and using high-order Hermite interpolation to reconstruct φ from both values and gradients [4, 27]. This enhances local geometric expressiveness and enables sub-grid accuracy, with extensions to phase-change simulations [2] and curvature-driven flows [26]. However, since GALS methods store and evolve information on fixed Eulerian grids, they still rely on grid-based interpolation during advection, which introduces cumulative errors over long time horizons. The above two classes of improvements—particle-based correction and gradient-augmented grid methods—address the limitations of classical level set methods from different angles, but neither fundamentally resolves the issue of accumulated interpolation errors inherent in local temporal updates.

1.1. Characteristic Map Methods

Rather than correcting errors locally at each time step, characteristic mapping methods [39, 70, 63] take a fundamentally different approach by maintaining long-range mappings that trace back to initial conditions. The key observation is that the

advection equation (2) admits a characteristic solution: along particle trajectories, the level set value is conserved. Specifically, if we define the forward flow map $\phi_{t_0 \rightarrow t}(\mathbf{X})$ as the mapping from the initial position \mathbf{X} at time t_0 to the current position \mathbf{x} at time t , satisfying

$$\frac{\partial \phi_{t_0 \rightarrow t}}{\partial t} = \mathbf{u}(\phi_{t_0 \rightarrow t}, t), \quad \phi_{t_0 \rightarrow t_0} = \mathbf{X}, \quad (5)$$

then the solution to the advection equation can be written as

$$\varphi(\mathbf{x}, t) = \varphi_0(\psi_{t \rightarrow t_0}(\mathbf{x})), \quad (6)$$

where $\psi_{t \rightarrow t_0}$ denotes the backward (inverse) flow map and φ_0 is the initial level set function. This formulation shows that, in principle, the level set value at any point and time can be obtained exactly by tracing back to the initial configuration without any numerical diffusion from repeated grid interpolation.

The concept of characteristic mapping builds upon semi-Lagrangian advection schemes [3, 57], which approximate the backward map over a single time step:

$$\varphi(\mathbf{x}, t^{n+1}) \approx \varphi(\mathbf{x} - \mathbf{u} \Delta t, t^n). \quad (7)$$

However, classical semi-Lagrangian methods construct this mapping only within a single time step, and repeated interpolation still introduces numerical dissipation. Long-range characteristic mapping methods [39, 70, 71] extend this concept by maintaining mappings over multiple time steps, storing the reference coordinates \mathbf{X} on grid nodes so that each grid point at time t records its original coordinates at time t_0 . Similarly, reference-map techniques [31] track material deformation through an Eulerian reference map $\xi(\mathbf{x}, t)$ and have demonstrated strong volume preservation for level set methods. Quantities can then be transported directly from the initial frame via Eq. (6), avoiding the accumulation of interpolation errors. This framework has also been combined with gradient-augmented formulations [62] for transport on spheres and other manifolds. However, since these methods store the mapping on fixed Eulerian grids, they still incur interpolation errors when evaluating the map at non-grid locations.

Particle Flow Map. To overcome the interpolation limitations of grid-based flow maps, the Particle Flow Map (PFM) method [75] builds upon the observation that Lagrangian particles inherently encode bidirectional flow maps without grid interpolation. Each particle stores both its current position $\mathbf{x}_p(t)$ and its initial position $\mathbf{X}_p = \mathbf{x}_p(t_0)$, thereby providing direct samples of both the forward map ϕ and the backward map ψ :

$$\mathbf{x}_p(t) = \phi_{t_0 \rightarrow t}(\mathbf{X}_p), \quad \mathbf{X}_p = \psi_{t \rightarrow t_0}(\mathbf{x}_p(t)). \quad (8)$$

To achieve higher-order accuracy, PFM also evolves the forward Jacobian $\mathcal{F}_p = \partial\phi_{t_0 \rightarrow t}/\partial\mathbf{X}$ along each particle trajectory:

$$\frac{d\mathcal{F}_p}{dt} = \nabla\mathbf{u}(\mathbf{x}_p, t) \cdot \mathcal{F}_p, \quad \mathcal{F}_p(t_0) = \mathbf{I}. \quad (9)$$

By discretizing the flow map into a set of Lagrangian particles that advect both position and Jacobian information, PFM obtains accurate flow maps implicitly without auxiliary computation or historical velocity buffers. The transfer of information between particles and the Eulerian grid follows the Affine Particle-In-Cell (APIC) style formulation [24], which enables particles to carry higher-order information transferred to grid nodes via weighted Taylor expansion $q_i = \sum_p [q_p + \nabla q_p \cdot (\mathbf{x}_i - \mathbf{x}_p)] \omega_{ip} / \sum_p \omega_{ip}$, reducing numerical dissipation and achieving high-order accuracy in long-range transport without global map reconstruction.

Recent developments have applied the particle flow map methods, both particle-based and grid-based, to transport impulse and other advected invariants across diverse fluid phenomena, including incompressible flows [75, 40, 11], compressible flows [6], vortical flows [68, 67], and solid-fluid coupling [5, 32]. Methodologically, extensions include Clebsch-gauge formulations [34], gradient-buffer-free transport [35], GPU-accelerated hybrid coupling [66], and differentiable simulation frameworks [33]. However, the application of particle flow maps to interface tracking problems, particularly level set methods with narrow-band confinement and high-order geometric preservation, remains unexplored.

Particle flow map methods achieve long-range transport accuracy through bidirectional flow maps, but have not been applied to level set interface tracking. In contrast to “virtual-particle” approaches [22, 12, 15, 13] that reconstruct flow trajectories through backward tracing incurring significant temporal buffering and sub-stepping overhead PFM establishes a compact, physically consistent bridge between Lagrangian advection and Eulerian projection. This motivates our central question: can we combine the high-order geometric representation of GALS with the long-range flow map accuracy of PFM to achieve high-fidelity level set advection while maintaining the efficiency of narrow-band formulations?

1.2. Particle Flow Map Level Set

Building upon these insights, we present a Particle Flow Map Level Set (PFM-LS) method for high-fidelity level-set interface tracking. By transporting φ , $\nabla\varphi$, and $\nabla^2\varphi$ on particles according to their respective differential forms, we achieve a high-order geometric representation that remains accurate under complex flow deformations. The proposed framework confines particles to a narrow band $\Omega_\epsilon = \{\mathbf{x} : |\varphi(\mathbf{x})| <$

$\epsilon\}$ around the interface, significantly reducing computational cost while focusing resources where accuracy is most critical. Each particle p stores the level-set value φ_p (transported as a 3-form), its gradient $\mathbf{g}_p = \nabla \varphi_p$ (transported as a 1-form), and Hessian $\mathbf{H}_p = \nabla^2 \varphi_p$. These quantities are transported along particle trajectories according to their respective differential structure:

$$\varphi_p(t) = \varphi_p(0), \quad \mathbf{g}_p(t) = \mathcal{T}_p^\top \mathbf{g}_p(0), \quad (10)$$

where the level set value is preserved along characteristics, and the gradient transforms via the transposed backward Jacobian \mathcal{T}_p^\top . The Hessian evolution involves higher-order derivatives of the flow map.

We reconstruct the level set field using APIC-style [24] interpolation with second-order Taylor expansion, leveraging the gradient and Hessian carried by each particle to capture sub-grid features such as thin filaments and small droplets. To control error accumulation over time, we adopt a dual-timescale flow map strategy: a long-range map preserves φ and $\nabla \varphi$ over extended periods, while a frequently reinitialized short-range map handles the distortion-sensitive Hessian. Since particles may disperse during advection, adaptive particle control dynamically generates new particles when local density falls below a threshold, ensuring sufficient coverage near evolving interfaces. Finally, to maintain the signed-distance property essential for curvature computation, we employ a hybrid particle-grid redistancing scheme that combines quasi-Newton projection with gradient-consistency blending, preserving fine-scale features captured by particles. Together, these components enable accurate reconstruction of complex interface geometries that are typically lost in conventional grid-based schemes.

Our method differs from existing approaches in two key aspects. First, unlike GALS and reference-map methods that store and evolve geometric information on fixed Eulerian grids, our method leverages particles to carry high-order geometric information through accurate long-range flow maps, avoiding the interpolation errors inherent in grid-based characteristic mapping. Second, unlike previous particle level set methods that use particles primarily to correct the level set function post hoc, our particles directly encode the interface geometry through their flow maps and higher-order derivative information, serving as the primary carriers of interface evolution rather than auxiliary correction tools.

The key contributions of our work include:

1. A framework that integrates particle-based tracking with flow maps to achieve fourth-order accurate interface representation and advection, where particles carry level set values φ , gradients \mathbf{g} , and Hessians \mathbf{H} that are transported exactly along characteristics.

2. A high-order particle-to-grid transfer scheme that preserves geometric information within a narrow band around the interface, using the transported derivatives to enable accurate Hermite interpolation during reconstruction.
3. An adaptive particle control mechanism that maintains consistent particle density near the interface during advection, including seeding, deletion, and redistribution strategies that preserve flow map accuracy.
4. A novel particle-based quasi-Newton projection method for redistancing that preserves fine-scale features during interface reconstruction, avoiding the smoothing typically introduced by PDE-based reinitialization.

The remainder of this paper is organized as follows. In Section 2, we present the mathematical background of our method, including level sets, gradient-augmented level sets, flow maps, and particle flow maps. Section 3 details our particle flow map approach for gradient-augmented level sets, covering advection, reconstruction, and narrow band implementation. Section 4 focuses on reinitialization procedures, including flow map reinitialization and our particle Newton redistancing method. Section 5 presents numerical results comparing our method against a wide range of existing approaches. Finally, Section 6 concludes with a discussion of our findings and directions for future work.

2. Mathematical Background

In this section, we present the mathematical foundations of our method, including level sets, gradient-augmented level sets, flow maps, and particle flow maps. We first establish the notation used throughout the paper in Table 1, then provide the necessary background on each concept.

2.1. Level Sets

In this paper, we focus on level set methods [45] for interface tracking between two materials in \mathbb{R}^2 . Without loss of generality, we denote materials as 0 (air) and 1 (liquid). The level set function $\varphi(\mathbf{x}, t)$ is defined in the entire domain and satisfies:

$$\varphi(\mathbf{x}, t) = \begin{cases} < 0, & \mathbf{x} \in \Omega_1, \\ = 0, & \mathbf{x} \in \partial\Omega, \\ > 0, & \mathbf{x} \in \Omega_0, \end{cases} \quad (11)$$

where Ω_1 represents the liquid region, Ω_0 represents the air region, and $\partial\Omega$ denotes the liquid-air interface, which is a codimension-1 geometric structure (i.e., a curve in \mathbb{R}^2 , or a surface in \mathbb{R}^3). This implicit representation enables direct computation of

Table 1: Summary of important notations used in the paper.

Notation	Type	Definition
φ	scalar	level set function
Ω_0	region	air domain ($\varphi > 0$)
Ω_1	region	liquid domain ($\varphi < 0$)
$\partial\Omega$	manifold	interface between materials ($\varphi = 0$)
$\nabla\varphi, \mathbf{g}$	vector	gradient of level set function
$\nabla^2\varphi, \mathbf{H}$	matrix	Hessian of level set function
\mathbf{n}	vector	unit normal vector at interface ($\frac{\nabla\varphi}{ \nabla\varphi }$)
\mathbf{v}, \mathbf{u}	vector	velocity field $(u, v, w)^T$
\mathbf{X}	vector	initial position of material point
\mathbf{x}	vector	current position of material point
ϕ	function	forward flow map from initial to current position
ψ	function	backward flow map from current to initial position
\mathcal{F}	matrix	Jacobian of forward flow map ϕ
\mathcal{T}	matrix	Jacobian of backward flow map ψ
$\mathcal{F}_{[c,a]}$	matrix	forward Jacobian from c to a
$\mathcal{T}_{[a,c]}$	matrix	backward Jacobian from a to c
ω	function	interpolation weight function

key geometric properties from the level set function. The unit normal vector at any point on the interface is given by $\mathbf{n} = \frac{\nabla\varphi}{|\nabla\varphi|}$, pointing from the liquid region toward the air region. The mean curvature is computed as $\kappa = \nabla \cdot \mathbf{n} = \nabla \cdot \left(\frac{\nabla\varphi}{|\nabla\varphi|} \right)$, which quantifies the local geometry of the interface. The evolution of the interface under a velocity field $\mathbf{v} = (u, v, w)^T$ is governed by the advection equation $\frac{\partial\varphi}{\partial t} + \mathbf{v} \cdot \nabla\varphi = 0$, which can be discretized using high-order ENO [54] or WENO schemes [36]. For numerical stability, φ should maintain the signed distance property $|\nabla\varphi(\mathbf{x})| = 1$. When this property deteriorates during evolution, reinitialization is performed by solving $\frac{\partial\varphi}{\partial\tau} = \text{sgn}(\varphi_0)(1 - |\nabla\varphi|)$ in pseudo-time τ , or alternatively using Fast Marching Method [49].

The standard level set method often suffers from numerical dissipation during advection. Enright et al. [12] addressed this by introducing marker particles near the interface $\varphi = 0$. These particles, with positions \mathbf{x}_p and radii r_p , are advected alongside the level set and help detect and correct interface errors when they cross the zero isocontour incorrectly. This hybrid approach demonstrates that incorporating particles into the level set framework is both natural and significantly improves

accuracy for complex interface dynamics.

Level Set Gradient. Nave et al. [41] introduced a method that maintains the level set’s gradient $\nabla\varphi$ as an auxiliary field and uses it to enhance the level-set function’s local expressiveness through high-order interpolation. This approach significantly improves the accuracy of the level set method and related interface property calculations, such as curvature. Li et al. [31] and Nave et al. [41] demonstrated that, with the aid of a fourth-order Hermite interpolation scheme on an Eulerian grid, they could better preserve droplets or thin films much smaller than the grid resolution. To reinitialize the gradient-augmented level set, quasi-Newton methods are typically employed to reinitialize both φ and $\nabla\varphi$ around the interface by iteratively solving for the nearest point on $\partial\Omega$.

2.2. Flow Map

Consider interfacial dynamics governed by a spatiotemporal velocity field $\mathbf{u}(\mathbf{q}, \tau)$ evolving from time 0 to time t . We denote the initial position of a material point as \mathbf{X} and its current position at time t as \mathbf{x} . The fluid motion over this time interval can be characterized by a forward flow map ϕ , defined as:

$$\begin{cases} \frac{\partial\phi(\mathbf{X}, \tau)}{\partial\tau} = \mathbf{u}[\phi(\mathbf{X}, \tau), \tau], \\ \phi(\mathbf{X}, 0) = \mathbf{X}, \\ \phi(\mathbf{X}, t) = \mathbf{x}. \end{cases} \quad (12)$$

The backward flow map ψ represents the inverse mapping of the forward flow map and is defined as:

$$\begin{cases} \phi(\psi(\mathbf{x}, \tau), \tau) = \mathbf{x}, \\ \psi(\mathbf{x}, 0) = \mathbf{x}, \\ \psi(\mathbf{x}, t) = \mathbf{X}. \end{cases} \quad (13)$$

We denote the Jacobian matrices of ϕ and ψ by \mathcal{F} and \mathcal{T} , respectively:

$$\mathcal{F}(\mathbf{X}, \tau) = \frac{\partial\phi(\mathbf{X}, \tau)}{\partial\mathbf{X}}, \quad \mathcal{T}(\mathbf{x}, \tau) = \frac{\partial\psi(\mathbf{x}, \tau)}{\partial\mathbf{x}}. \quad (14)$$

As proven in [19], the temporal evolution of \mathcal{F} and \mathcal{T} is described by:

$$\frac{\partial\mathcal{F}}{\partial t} = \nabla\mathbf{u}\mathcal{F}, \quad \frac{D\mathcal{T}}{Dt} = -\mathcal{T}\nabla\mathbf{u}. \quad (15)$$

$\frac{D(\cdot)}{Dt}$ represents the material derivative, which describes the rate of change of the Jacobians moving with the particle along its flow map’s trajectory.

2.3. Particle Flow Map

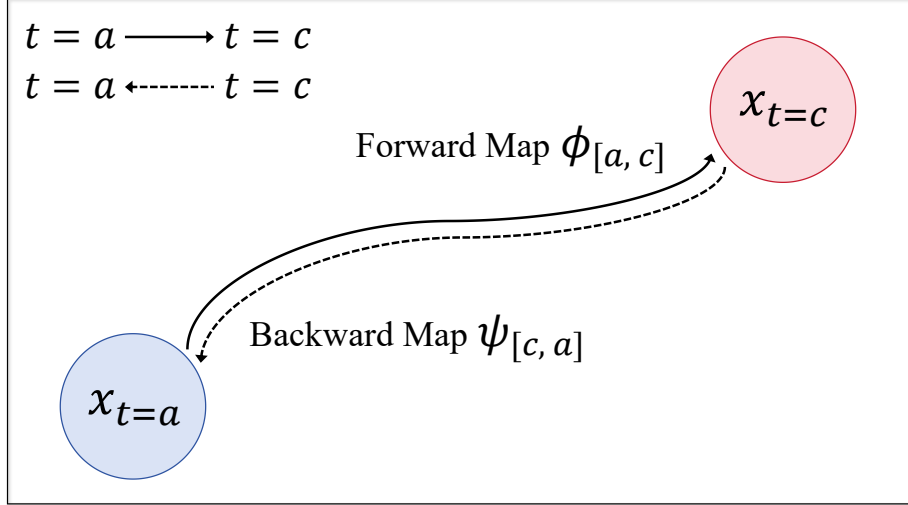


Figure 1: Particle trajectory from time a to c naturally defines both forward map $\phi_{[a,c]}$ and backward map $\psi_{[c,a]}$, forming a perfect bidirectional flow map.

Building upon the flow map concept, Zhou et al. [75] observed that particle trajectories naturally embody bidirectional flow maps. When a particle moves according to velocity field $\mathbf{u}(\mathbf{x}, t)$, its path from time a to time c defines both the forward map $\phi_{[a,c]}$ and the backward map $\psi_{[c,a]}$ as in figure 1. A particle flow map constitutes a perfect flow map by naturally satisfying bidirectionality requirements. A particle moving from \mathbf{X} at time 0 to \mathbf{x} at time t via $\phi(\mathbf{X}, t)$ will follow the same trajectory in reverse when moving according to $\psi(\mathbf{x}, t)$. The Jacobians defined in Equation (15) can be directly evaluated along these trajectories, providing an efficient method for tracking deformations in complex systems.

Geometric Insight: Transport of Differential Forms on Particles. The success of the Particle Flow Map methods stems from a unified geometric principle: different physical quantities transform according to their differential structure under flow map transport (see Figure 2 and Table 2). We summarize the three canonical cases: (1) *Point elements (3-forms):* Scalar quantities such as density [56, 13] are preserved along trajectories:

$$\frac{D\rho}{Dt} = 0, \quad \rho(t) = \rho(0). \quad (16)$$

	Surface Elements (1-forms)	Line Elements (2-forms)	Point Elements (3-forms)
Evolution	$\frac{D\mathbf{s}}{Dt} = -(\nabla \mathbf{u})^\top \mathbf{s}$	$\frac{D\mathbf{l}}{Dt} = (\nabla \mathbf{u}) \mathbf{l}$	$\frac{D\rho}{Dt} = 0$
Flow Map	$\mathbf{s}(t) = T^\top \mathbf{s}(0)$	$\mathbf{l}(t) = F \mathbf{l}(0)$	$\rho(t) = \rho(0)$
Example	impulse [9, 40, 14, 11, 75]	vorticity [67, 68]	density [56, 13]

Table 2: Differential forms and their transformation under flow maps. The level set value φ is transported as a 3-form (point element), while the gradient $\nabla\varphi$ is transported as a 1-form (surface element).

$$t = 0 \longrightarrow t = T \quad t = 0 \leftarrow \cdots t = T$$

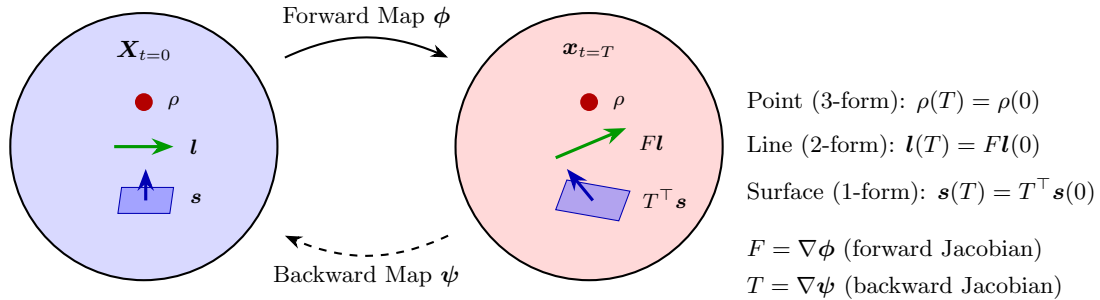


Figure 2: Transport of differential forms under the flow map. Point elements (3-forms, e.g., ρ) are preserved; line elements (2-forms, e.g., vorticity) transform via $F = \nabla\phi$; surface elements (1-forms, e.g., impulse) transform via T^\top .

(2) *Line elements (2-forms)*: Quantities such as vorticity [67, 68] stretch and rotate via the velocity gradient:

$$\frac{D\mathbf{l}}{Dt} = (\nabla \mathbf{u}) \mathbf{l}, \quad \mathbf{l}(t) = \mathcal{F} \mathbf{l}(0). \quad (17)$$

(3) *Surface elements (1-forms)*: Quantities such as impulse [9, 40, 14, 11, 75] transform via the transposed Jacobian:

$$\frac{D\mathbf{s}}{Dt} = -(\nabla \mathbf{u})^\top \mathbf{s}, \quad \mathbf{s}(t) = \mathcal{T}^\top \mathbf{s}(0). \quad (18)$$

A key observation is that the gradient of a 3-form yields a 1-form. This principle directly applies to level set methods: the level set value φ is a scalar (3-form) preserved along characteristics, and its gradient $\nabla\varphi$ transforms as a 1-form—precisely

analogous to the relationship between density and impulse. This observation is consistent with GALS methods [42], which evolve both φ and $\nabla\varphi$ as independent variables, but interprets them through the lens of differential forms. Understanding level set advection in this way allows us to unify interface tracking within the PFM framework:

$$\varphi(t) = \varphi(0), \quad \nabla\varphi(t) = \mathcal{T}^\top \nabla\varphi(0). \quad (19)$$

3. Level Set on Particle Flow Maps

We use the particle flow map to track the level set φ and its higher-order information gradient $\nabla\varphi$ and hessian $\nabla^2\varphi$. As mentioned in [75], a perfect flow map can maintain exceptionally high accuracy during advection, and particles naturally follow a perfect flow map. As illustrated in Figure 3, particles carrying both level set values and higher gradient information provide an APIC-style [24] high-order interpolation that significantly enhances the representation of sub-grid features. This approach allows our method to preserve fine structures such as small droplets and thin films during advection, even when these features are smaller than the grid resolution.

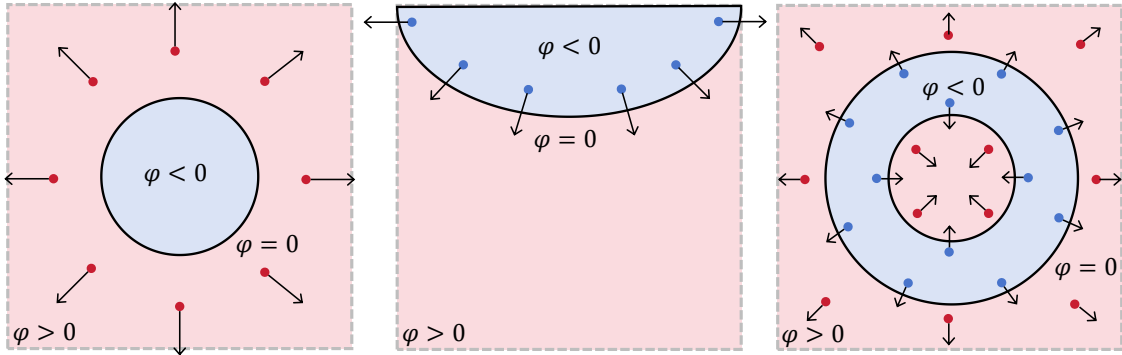


Figure 3: Illustration of gradient-augmented level sets with particles. Red and blue particles carry level set values and gradient information (arrows) near the interface $\varphi = 0$. This higher-order representation enables capturing sub-grid features such as small droplets (left), thin films (middle), and annular structures (right) that traditional methods cannot resolve.

3.1. Particle Advection

We now describe how to advect the level set function φ , its gradient $\nabla\varphi$, and its Hessian $\nabla^2\varphi$ using particle flow maps. The level set value is directly conserved along particle trajectories. Given the backward flow map $\psi(\mathbf{x}, t)$, the advection follows:

$$\varphi(\mathbf{x}, t) = \varphi(\psi(\mathbf{x}, t), 0) \quad (20)$$

For the gradient field, let $\mathbf{g} = \nabla\varphi$ denote the gradient. Using the transpose of the backward deformation gradient:

$$\mathbf{g}(\mathbf{x}, t) = \mathcal{T}_t^T(\mathbf{x})\mathbf{g}(\psi(\mathbf{x}, t), 0) \quad (21)$$

where $\mathcal{T}_t(\mathbf{x}) = \frac{\partial\psi(\mathbf{x}, t)}{\partial\mathbf{x}}$ is the Jacobian of the backward flow map. For the Hessian matrix, let $\mathbf{H} = \nabla^2\varphi$ denote the Hessian. The transformation incorporates both deformation and its spatial variation:

$$\mathbf{H}(\mathbf{x}, t) = \mathcal{T}_t^T \nabla_\psi \mathbf{g}(\psi(\mathbf{x}, t), 0) \mathcal{T}_t + \nabla \mathcal{T}_t^T \mathbf{g}(\psi(\mathbf{x}, t), 0) \quad (22)$$

where ∇_ψ denotes the gradient with respect to the variable ψ . In practice, we use an approximate form

$$\mathbf{H}(\mathbf{x}, t) \approx \mathcal{T}_t^T \nabla_\psi \mathbf{g}(\psi(\mathbf{x}, t), 0) \mathcal{T}_t, \quad (23)$$

since as indicated in [75], the calculation of $\nabla \mathcal{T}_t$ is challenging due to its high-order nature. The authors propose to leave this term out of the calculation due to the observation that the Hessian mostly depends on the first term.

By tracking these three quantities using particle flow maps, we achieve a higher-order representation that maintains geometric fidelity during complex interface deformations. While the perfect flow map approach provides high accuracy, numerical errors can accumulate over time. To balance accuracy and efficiency, we implement a dual-timescale flow map approach. We store two backward Jacobians: $\mathcal{T}_{[a,b]}$ and $\mathcal{T}_{[b,c]}$, where a is the initial time, c is the current time, and b is an intermediate time closer to c . The long backward Jacobian $\mathcal{T}_{[a,c]}$ can be computed as $\mathcal{T}_{[a,c]} = \mathcal{T}_{[a,b]} \mathcal{T}_{[b,c]}$. At each time step, we update the short-range flow map by marching $\mathcal{T}_{[b,c]}$ by one step in parallel with the particle's advection, using our custom 4th order of Runge-Kutta (RK4) integration scheme. Subsequently, the long-range flow map is updated according to $\mathcal{T}_{[a,c]} = \mathcal{T}_{[a,b]} \mathcal{T}_{[b,c]}$, with $\mathcal{T}_{[a,b]}$ which has been reinitialized at time b . The long flow map is used for advecting the level set value φ and its gradient $\nabla\varphi$, while the short flow map is used for the Hessian $\nabla^2\varphi$, which is more sensitive to flow distortion. Details of the flow map reinitialization process are presented in Section 4.1.

Next, we will describe how to utilize the level set value φ , gradient \mathbf{g} , and Hessian \mathbf{H} stored on particles to interpolate and reconstruct a highly accurate, feature-preserving level set function throughout the computational domain.

3.2. Grid Reconstruction

Having tracked the level set values, gradients, and Hessians on particles through advection, we now need to reconstruct the continuous level set field throughout the domain. To leverage the higher-order information carried by particles, we adopt an

APIC-style [24] interpolation approach. For any query point \mathbf{x}_α in the domain, we reconstruct the level set value using a second-order Taylor series expansion:

$$\varphi_\alpha = \frac{\sum_{p \in N_\alpha} [\varphi_p + \mathbf{g}_p \cdot (\mathbf{x}_\alpha - \mathbf{x}_p) + \frac{1}{2}(\mathbf{x}_\alpha - \mathbf{x}_p)^T \mathbf{H}_p (\mathbf{x}_\alpha - \mathbf{x}_p)] \omega(\mathbf{x}_p, \mathbf{x}_\alpha)}{\sum_{p \in N_\alpha} \omega(\mathbf{x}_p, \mathbf{x}_\alpha)} \quad (24)$$

where $N_\alpha = \{p \in P \mid \omega(\mathbf{x}_p, \mathbf{x}_\alpha) > 0\}$ represents the set of particles in the neighborhood of query point α , and $\omega(\mathbf{x}_p, \mathbf{x}_\alpha)$ is the interpolation weight that decreases with distance. Similarly, for the gradient field \mathbf{g}_α at the query point, we use a first-order Taylor series expansion of the gradient:

$$\mathbf{g}_\alpha = \frac{\sum_{p \in N_\alpha} [\mathbf{g}_p + \mathbf{H}_p (\mathbf{x}_\alpha - \mathbf{x}_p)] \omega(\mathbf{x}_p, \mathbf{x}_\alpha)}{\sum_{p \in N_\alpha} \omega(\mathbf{x}_p, \mathbf{x}_\alpha)} \quad (25)$$

These formulations naturally extend our particle-based flow map approach by incorporating both gradient and second-order derivative information in the reconstruction process. The first-order term $\mathbf{g}_p \cdot (\mathbf{x}_\alpha - \mathbf{x}_p)$ captures local directional changes, while the second-order term $\frac{1}{2}(\mathbf{x}_\alpha - \mathbf{x}_p)^T \mathbf{H}_p (\mathbf{x}_\alpha - \mathbf{x}_p)$ accounts for the local variations in the gradient of the level set field. This higher-order reconstruction preserves sharp features and complex interface geometries that would otherwise be lost with standard interpolation methods, aligning with our goal of maintaining the high accuracy promised by the perfect flow map described in Section 3.1.

3.3. Narrow Band

While the level set method provides an elegant framework for interface tracking, only the level set values near the interface are critical for capturing the interface geometry. Inspired by [12] and [15], we enhance our PFM-LS approach by adopting a narrow band strategy, which focuses computational resources where they matter most. We define the narrow band as a region of width $n\Delta x$ surrounding the interface, where n typically ranges from 1 to 4 in our experiments and Δx represents the length of the background grid. As shown in Figure 4, our method concentrates particles only near the interface, tracking their level set values, gradients, and Hessians through the backward flow map $\psi_{[c,a]}$. This narrow band approach significantly reduces computational cost while maintaining high accuracy where it matters most. This focused approach offers significant advantages over traditional flow maps or reference maps [11, 31]. Specifically, the particle flow map naturally aligns with this narrow band concept, as we only need to maintain particles within this region of interest.

The narrow band particle flow map substantially reduces memory requirements and computational overhead compared to a full-domain approach. Outside the narrow band, where high interface accuracy is not needed, we use a standard grid-based

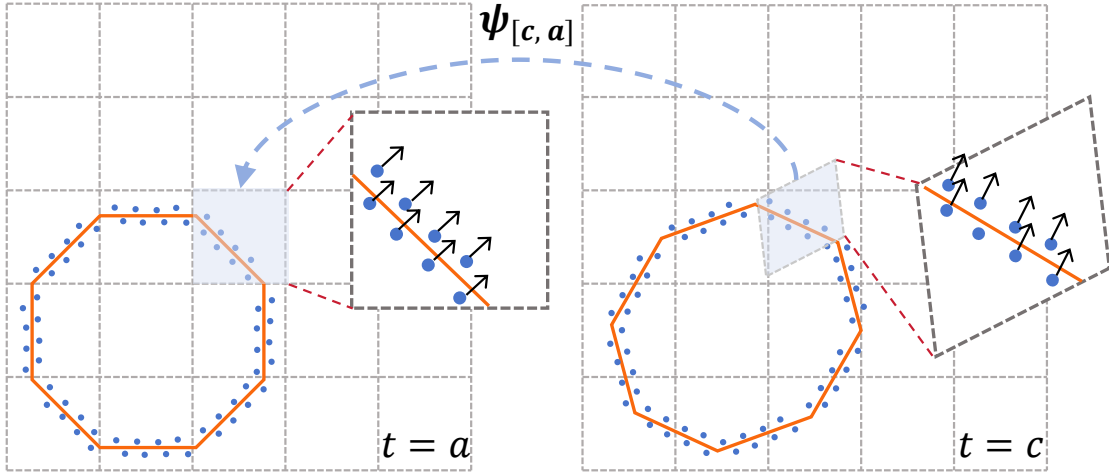


Figure 4: Narrow band particle flow map level set representation. The octagonal interface (orange) is tracked by particles (blue dots) concentrated only in a narrow band around the interface. The zoomed regions show particles carrying gradient information (arrows) at two time points, with the backward map $\psi_{[c, a]}$ connecting their positions. This focused approach maintains high accuracy near the interface while reducing computational cost elsewhere.

representation of the level set with conventional semi-Lagrangian advection. To ensure continuity of the level set field across the entire domain, we apply a smooth transition within a small region ($1\Delta x$ width) at the boundary between the narrow band and background grid. In this transition region, we blend the values as $\varphi_{\text{cross}} = w \cdot \varphi_{\text{particle}} + (1 - w) \cdot \varphi_{\text{grid}}$, where w is a blending weight that linearly decreases from 1 at the inner boundary to 0 at the outer boundary of this transition region. Since these transition regions are far from the interface, minor interpolation inaccuracies have a negligible impact on interface dynamics.

A challenge with particle flow maps is that particles may accumulate or disperse near the interface during advection if not reinitialized frequently, leading to non-uniform particle distribution and potential accuracy degradation. While Zhou et al. [75] uses particle flow maps for impulse advection, which inherently requires more frequent reinitialization than level sets, PFM for level sets can maintain longer flow periods with fewer reinitializations to better preserve interface features. Additionally, unlike [75], which needs particles spread across the entire domain, our narrow band PFM only maintains particles within the narrow band region. This concentration of particles makes Narrow band PFM-LS more susceptible to particle dispersion near the interface, precisely where adequate particle density is most critical for accuracy. To address this issue, we implement adaptive particle control similar to the approach

in NBFLIP [15], which dynamically manages particle density to maintain consistent accuracy throughout the simulation. The details of this adaptive particle control mechanism will be presented in the following section.

3.4. Adaptive Particle Control

A key challenge in the narrow-band PFM-LS framework is maintaining sufficient particle density near the interface during advection. Standard PFM implementations [75, 5, 32] rely on periodic flow-map reinitialization (Section 4) to restore uniform coverage, but particle loss within the narrow band between reinitializations can degrade accuracy. To address this, we introduce an adaptive particle control mechanism.

A background grid, matching the simulation resolution, monitors particle counts in each narrow-band cell. We define a minimum threshold n_{\min} —typically half of the reinitialization density—and dynamically generate new particles when the count drops below n_{\min} . Particles are not deleted, as overpopulation is naturally corrected during the next reinitialization. For each newly generated particle, the level-set value φ and gradient \mathbf{g} are interpolated from nearby particles using the APIC-style scheme (Section 3.2). The Hessian \mathbf{H} is estimated via finite differences of the reconstructed gradient field, improving accuracy over direct interpolation. The flow-map Jacobians \mathcal{T}_p and \mathcal{F}_p are initialized as identity matrices since the particles are created within the current time step.

This adaptive control maintains adequate particle coverage near evolving interfaces and focuses computation where accuracy is most critical, achieving a robust balance between precision and efficiency.

4. Reinitialization

Our PFM-LS framework employs two complementary reinitialization procedures to maintain numerical stability and signed-distance accuracy: (1) *flow-map reinitialization*, which regenerates particles and resets flow maps; and (2) *level-set redistancing*, which enforces the signed-distance property of φ . We detail both processes and their execution criteria below.

4.1. Flow-Map Reinitialization

Flow-map methods accumulate numerical errors over time and require periodic reinitialization to preserve accuracy. Following the single-sample long–short flow map scheme of Zhou et al. [75], we maintain two coupled flow maps between initial time a and current time c with an intermediate timestamp b ($a < b < c$). This produces a long flow map $[a, c]$ and a short flow map $[b, c]$, with corresponding backward

Jacobians $\mathcal{T}_{[a,b]}$ and $\mathcal{T}_{[b,c]}$. The full backward map is obtained as $\mathcal{T}_{[a,c]} = \mathcal{T}_{[a,b]}\mathcal{T}_{[b,c]}$. We use the long map for advecting φ and $\nabla\varphi$, while the short map—reinitialized more frequently—is used for $\nabla^2\varphi$, which is more sensitive to flow distortion.

Long-range reinitialization.. Performed every f_L time steps (typically 50), it:

1. Uniformly redistributes particles within the narrow band (e.g., 4×4 per cell).
2. Resets all Jacobians $\mathcal{T}_{[a,b]}, \mathcal{T}_{[b,c]}, \mathcal{F}_{[a,b]}, \mathcal{F}_{[b,c]}$ to identity.
3. Updates the initial time reference to the current frame.
4. Interpolates φ , $\nabla\varphi$, and $\nabla^2\varphi$ to new particle positions using the adaptive interpolation in Section 3.4; if combined with redistancing, blending is applied as in Section 4.3.

Short-range reinitialization.. Executed every f_S steps (typically 5), it:

1. Resets $\mathcal{T}_{[b,c]}$ and $\mathcal{F}_{[b,c]}$ to identity.
2. Recomputes Hessians $\nabla^2\varphi$ at current particle positions.

This hierarchical reinitialization strategy effectively balances accuracy and efficiency by stabilizing long-term flow-map evolution while preserving fine-scale curvature information.

4.2. Level-set Redistancing

During advection, the level-set function gradually deviates from the signed-distance property ($|\nabla\varphi| = 1$), which is essential for accurate computation of interface normals and curvature. Existing redistancing techniques include fast marching methods [49], PDE-based WENO schemes [36, 25], and particle-based corrections [12]. We adopt a modified quasi-Newton redistancing scheme that cooperates between particles and the background grid. Instead of redistancing every particle—which is computationally expensive due to their high density near the interface—we redistribute grid nodes within the narrow band and transfer this information to particles through a subsequent flow-map reinitialization.

The redistancing frequency follows the same schedule as the long-range flow-map reinitialization. For applications such as liquid simulation that can tolerate small deviations from the signed-distance condition, a lower frequency or adaptive strategy [31] is recommended.

Our procedure consists of four stages:

1. **Initial guess:** Apply WENO iterations to obtain an initial φ field for grid points within the narrow band.

2. **Quasi-Newton projection:** For each grid node, perform a quasi-Newton projection onto the closest interface point following [31]. Each iteration includes (i) a gradient-descent step along $\nabla\varphi$, (ii) a perpendicular correction to align $(\mathbf{x} - \mathbf{x}_i)$ with $\nabla\varphi$, and (iii) a back-and-forth midpoint update to suppress oscillations. We replace grid-based Hermite interpolation with particle-based APIC-style interpolation for evaluating φ and $\nabla\varphi$, significantly improving sub-grid feature preservation and projection accuracy.
3. **Background propagation:** Extend the redistanced φ values from the narrow band to the background domain Ω_0 using a semi-Lagrangian Eikonal solver.
4. **Particle update:** Reinitialize particle flow maps and redistribute particles, transferring grid-based φ and $\nabla\varphi$ values through the hybrid blending strategy (Section 4.3).

This hybrid particle–grid formulation preserves the signed-distance property while maintaining fine-scale interface features. By performing redistancing on grid nodes rather than individual particles, it achieves substantial computational savings without compromising accuracy.

4.3. Hybrid Particle–Grid Blending

Following quasi-Newton redistancing, accurate level-set values are available on narrow-band grid nodes and must be transferred to redistributed particles. Neither pure grid interpolation nor exclusive use of particle values yields optimal accuracy, particularly for fine-scale features. We therefore employ a hybrid blending scheme that combines the stability of grid interpolation with the sub-grid fidelity of particle data. The insight is that grid-based Hermite interpolation performs well in well-resolved regions, whereas particles better capture small droplets and thin filaments below grid resolution. However, after several advection steps, particle values can drift, with distortion increasing away from the interface. To address this, we blend grid and particle contributions based on both proximity and gradient consistency. For particles within $0.25\Delta x$ of the interface, we compute the gradient consistency measure $\gamma = \frac{\nabla\varphi_p \cdot \nabla\varphi_g}{\|\nabla\varphi_p\| \|\nabla\varphi_g\|}$, where subscripts p and g denote particle- and grid-interpolated gradients. Blending weights are determined as follows:

- $\gamma > e_1 = 0.9$: adopt grid values;
- $e_2 = 0.7 < \gamma \leq e_1$: linearly blend grid and particle values;
- $\gamma \leq e_2$: retain particle values.

Algorithm 1 Particle Newton Redistancing

Require: Level set field φ , gradient field $\nabla\varphi$, narrow band region

Ensure: Redistanced level set with $|\nabla\varphi| = 1$ while preserving features

- 1: Initialize grid points with WENO iterations for initial guess
- 2: **for** each grid point \mathbf{x}_p in narrow band **do**
- 3: Apply quasi-Newton projection to find the closest interface point:
- 4: Initial guess: $\mathbf{x}_0 = \mathbf{x}_p - \varphi(\mathbf{x}_p) \frac{\nabla\varphi(\mathbf{x}_p)}{|\nabla\varphi(\mathbf{x}_p)|}$
- 5: Gradient-descent: $\mathbf{x}_{k+1/2} = \mathbf{x}_k - \frac{\varphi(\mathbf{x}_k) \nabla\varphi(\mathbf{x}_k)}{|\nabla\varphi(\mathbf{x}_k)|^2}$
- 6: Perpendicular adjustment: $\mathbf{x}_{k+1} = \mathbf{x}_{k+1/2} + \alpha(\mathbf{I} - \mathbf{n}\mathbf{n}^T)(\mathbf{x}_p - \mathbf{x}_{k+1/2})$
- 7: If $|\mathbf{x}_{k+1} - \mathbf{x}_{k-1}| < |\mathbf{x}_{k+1} - \mathbf{x}_k|$: $\mathbf{x}_{k+1} = \frac{1}{2}(\mathbf{x}_k + \mathbf{x}_{k+1})$
- 8: Update: $\varphi(\mathbf{x}_p) = \text{sgn}(\varphi_0)|\mathbf{x}_p - \mathbf{x}_k|$, $\nabla\varphi(\mathbf{x}_p) = \frac{\mathbf{x}_p - \mathbf{x}_k}{|\mathbf{x}_p - \mathbf{x}_k|}$
- 9: **end for**
- 10: Propagate values from narrow band to background regions
- 11: Apply hybrid particle-grid blending: ▷ Section 4.3
- 12: Compute $\gamma = \frac{\nabla\varphi_{\text{particle}} \cdot \nabla\varphi_{\text{grid}}}{|\nabla\varphi_{\text{particle}}||\nabla\varphi_{\text{grid}}|}$ for each particle
- 13: Blend based on γ and proximity to interface
- 14: Perform particle flow map reinitialization: ▷ Section 4.1
- 15: Redistribute particles in narrow band (e.g., 4×4 per cell)
- 16: Reset Jacobians: $\mathcal{T}_{[a,b]} \leftarrow \mathbf{I}$, $\mathcal{T}_{[b,c]} \leftarrow \mathbf{I}$
- 17: Update time references: $a \leftarrow c$
- 18: Interpolate φ_p , $\nabla\varphi_p$, $\nabla^2\varphi_p$ to new particles using APIC-style interpolation

This adaptive blending preserves fine-scale interface structures while maintaining global smoothness, outperforming both purely grid- and particle-based transfers, especially for thin filaments and small droplets. The complete redistancing and blending procedure is summarized in Algorithm 4.2.

4.4. Time Integration

We now summarize the complete time-stepping procedure that integrates all components of our particle flow map level set method. Each simulation step proceeds through four stages, as illustrated in Algorithm 2.

Stage 1: Flow Map Reinitialization. At the beginning of each step, we check whether reinitialization is required. Long-range reinitialization (every n^L steps, typically 50) redistributes particles uniformly within the narrow band and resets $\mathcal{T}_{[a,b]}$ to identity. Short-range reinitialization (every n^S steps, typically 5) resets $\mathcal{T}_{[b,c]}$ and recomputes the Hessian $\nabla^2\varphi$ to control curvature error accumulation.

Algorithm 2 Particle Flow Map Level Set Method

```

1: Initialize:  $\varphi_0, \nabla\varphi_0, \nabla^2\varphi_0$  to initial level set data;  $\mathcal{T}_{[a,b]}, \mathcal{T}_{[b,c]}$  to  $\mathbf{I}$ 
2: for  $k$  in total steps do
3:    $j \leftarrow k \bmod n^L$ ;                                 $\triangleright$  Long flow map counter
4:    $l \leftarrow k \bmod n^S$ ;                                 $\triangleright$  Short flow map counter
5:   if  $j = 0$  then
6:     Redistribute particles in narrow band;
7:     Reinitialize  $\varphi_p, \nabla\varphi_p, \nabla^2\varphi_p$ ;            $\triangleright$  Section 3.2
8:     Reinitialize  $\mathcal{T}_{[a,b]}$  to  $\mathbf{I}$ ;                       $\triangleright$  Section 4.1
9:   end if
10:  if  $l = 0$  then
11:    Reinitialize  $\nabla^2\varphi_p$ ;                          $\triangleright$  Section 3.1
12:    Reinitialize  $\mathcal{T}_{[b,c]}$  to  $\mathbf{I}$ ;                       $\triangleright$  Section 4.1
13:  end if
14:  Compute velocity  $\mathbf{u}$  at particle positions;
15:  Advect particles with RK4;
16:  Update  $\mathcal{T}_{[b,c]}$  with velocity gradient;            $\triangleright$  Eq. (15)
17:  Compute  $\mathcal{T}_{[a,c]}$  with  $\mathcal{T}_{[a,b]}$  and  $\mathcal{T}_{[b,c]}$ ;            $\triangleright$  Section 3.1
18:  Update  $\nabla\varphi_p$  with  $\mathcal{T}_{[a,c]}^T \nabla\varphi_0$ ;            $\triangleright$  Section 3.1
19:  Update  $\nabla^2\varphi_p$  with  $\mathcal{T}_{[b,c]}^T \nabla^2\varphi_0 \mathcal{T}_{[b,c]}$ ;            $\triangleright$  Section 3.1
20:  Check particle density in narrow band cells;
21:  Add new particles where density is below threshold;       $\triangleright$  Section 3.4
22:  Reconstruct  $\varphi$  on grid using APIC-style interpolation (if needed);       $\triangleright$ 
    Section 3.2
23:  if timeForRedistancing then
24:    Perform particle Newton redistancing;                   $\triangleright$  Section 4.2
25:  end if
26: end for

```

Stage 2: Advection and Flow Map Update. Particles are advected using fourth-order Runge-Kutta integration. Simultaneously, the short-range Jacobian $\mathcal{T}_{[b,c]}$ is updated by integrating Eq. (15). The long-range Jacobian is then computed as $\mathcal{T}_{[a,c]} = \mathcal{T}_{[a,b]} \mathcal{T}_{[b,c]}$, and the gradient $\nabla\varphi$ is updated via $\mathbf{g}_p = \mathcal{T}_{[a,c]}^T \mathbf{g}_p(0)$.

Stage 3: Particle Management. Adaptive particle control (Section 3.4) monitors particle density in narrow-band cells and generates new particles where coverage falls below the threshold n_{\min} . The level set field is then reconstructed on the grid using APIC-style interpolation (Section 3.2) when needed for visualization or external

coupling.

Stage 4: Redistancing. When the signed-distance property degrades beyond acceptable tolerance, particle Newton redistancing (Section 4.2) is performed, followed by hybrid particle-grid blending (Section 4.3) to restore $|\nabla\varphi| = 1$ while preserving fine-scale features.

5. Numerical Tests

In this section, we evaluate the performance of our method through various numerical experiments. We begin with advection tests in both 2D and 3D settings to assess the accuracy of our approach compared to existing methods. Throughout these tests, we measure the accuracy by tracking the area (2D) or volume (3D) of the level-set regions. For 2D area calculations, we sum the areas of triangles generated by marching squares on a grid that is four times finer than the original grid in each dimension. In 3D, we evaluate the liquid volume using the fast marching cubes-style scheme proposed by Takahashi and Batty [61]. Table 3 summarizes the methods compared in our experiments. We include several semi-Lagrangian advection schemes with varying interpolation orders: Linear (first-order), Quadratic, and Cubic. For each of these, we also test reference map-augmented versions (denoted with "+RM" suffix). Additionally, we compare against BFECC [48], Gradient-Augmented Level-Set (GALS) [41], Particle Level-Set (PLS) [12], GARM-LS [31], which combines GALS with reference maps, and Narrow Band FLIP (NBFLIP) [15]. For particle-based methods such as PLS($\times 16$) and our approach, the notation in parentheses indicates the number of particles initially seeded within each near-interface grid cell. For NBFLIP, we use 16 particles per cell in 2D and 64 particles per cell in 3D (with 4 particles aligned along each axis).

For pure advection tests, we focus solely on the advection capabilities. As such, we disable redistancing for all methods except PLS and NBFLIP, which require redistancing as an intrinsic part of their methodology. Our method performs regular flow map reinitialization as described in Section 4.1. In later tests, we also evaluate the effectiveness of our redistancing approach and compare the combined advection-redistancing performance against other methods.

All 2D tests are conducted within a domain of $[0, 1]^2$, while 3D tests are performed in a domain of $[0, 1]^3$. To ensure temporal accuracy across all methods, we employ a consistent time step size of $\Delta t = 0.02$ s. For grid-based methods, we utilize a fourth-order Runge–Kutta integration scheme to guarantee fair comparison of advection performance.

Table 3: Summary of methods compared in our experiments.

Method	Description
Linear	First-order semi-Lagrangian advection [57]
Linear+RM	First-order semi-Lagrangian with reference map
Quadratic	Second-order semi-Lagrangian advection
Quadratic+RM	Second-order semi-Lagrangian with reference map
Cubic	Third-order semi-Lagrangian advection [13]
Cubic+RM	Third-order semi-Lagrangian with reference map
BFECC	Back and Forth Error Compensation and Correction [48]
BFECC+RM	BFECC with reference map augmentation
GALS	Gradient-Augmented Level-Set method [41]
GARM-LS	Gradient-Augmented Reference Map Level-Set [31]
PLS($\times 16$)	Particle Level-Set with 16 particles per near-interface cell [12]
PLS($\times 36$)	Particle Level-Set with 36 particles per near-interface cell [12]
NBFLIP	Narrow Band FLIP method (x16 particles in 2D, x64 in 3D)[15]
Ours($\times 16$)	Our method with 16 particles per near-interface cell
Ours($\times 36$)	Our method with 36 particles per near-interface cell

5.1. 2D Zalesak’s disk

Zalesak’s disk test [72] is a widely recognized benchmark for evaluating advection schemes in preserving sharp interfaces at different orientations. This challenging test involves rotating a slotted disk in a prescribed velocity field, with the goal of returning to its initial configuration after one or more complete revolutions.

We adapt classical Zalesak’s disk setup to our domain of $[0, 1]^2$. The slotted disk has a radius of 0.15 and is initially centered at $(0.5, 0.5)$. The slot has dimensions of 0.05 by 0.25. To create a rotational velocity field, we define:

$$u = -\omega(y - 0.5), \quad v = \omega(x - 0.5) \quad (26)$$

where $\omega = \frac{\pi}{157 \cdot \Delta t}$ is the angular velocity. This configuration completes a full revolution at $T = 6.28$ seconds. All simulations were performed on a 200×200 grid.

Figure 5 compares various interface tracking methods in Zalesak’s disk rotation test. Our proposed narrow band particle flow map method demonstrates superior performance in both volume conservation and geometric preservation.

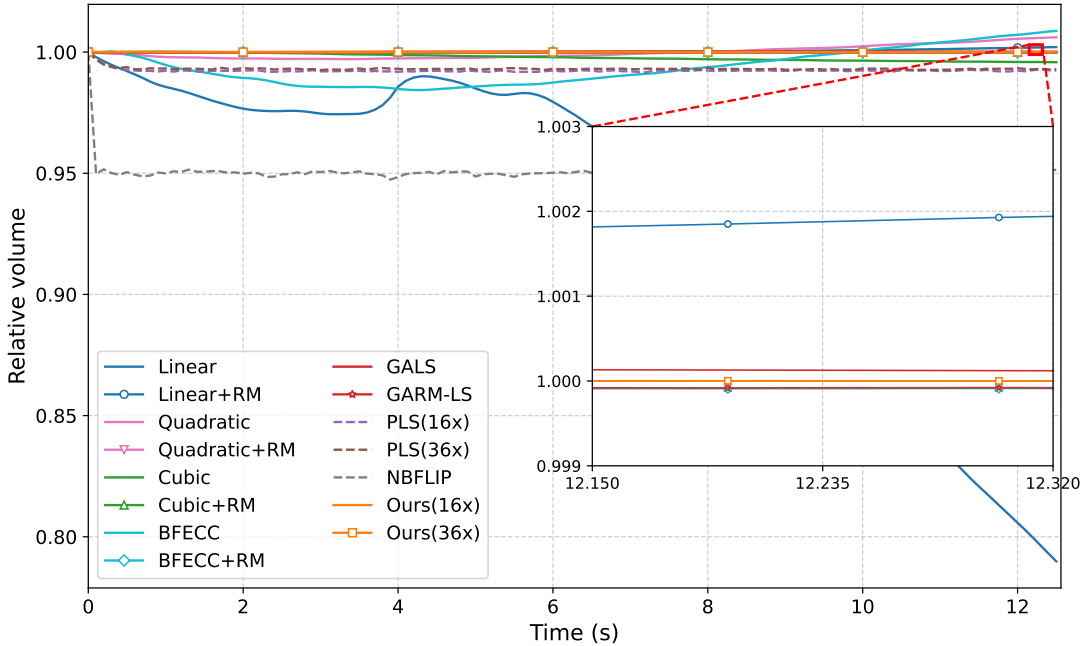


Figure 5: Volume preservation comparison during 200×200 **2D Zalesak's disk rotation test**. Our method (orange lines) maintains nearly perfect volume conservation throughout the entire revolution. The inset shows detailed performance during the final moments, where our method preserves over 99.9999% of the original volume, significantly outperforming all other methods. Most reference map-augmented methods (RM suffix) achieve good preservation, while traditional methods like Linear show substantial volume loss. Note that NBFLIP struggles in this test despite its particle-based nature.

Table 4 quantifies the relative volume error for each method. The first-order linear scheme exhibits substantial volume loss with a relative error of 2.12×10^{-1} . Higher-order methods show improvement, with quadratic, cubic, and BFECC methods achieving errors of 6.7×10^{-3} , 4.2×10^{-3} , and 8.9×10^{-3} , respectively. Reference map augmentation consistently reduces these errors, with Linear+RM showing dramatic improvement to 2.1×10^{-3} . Advanced level set methods (GALS and GARM-LS) perform well with errors of approximately 1.1×10^{-4} and 1.8×10^{-5} . The Particle Level-Set (PLS) method shows moderate volume loss despite its marker particle correction, with PLS($16\times$) and PLS($36\times$) configurations yielding errors of 7.59×10^{-3} and 7.13×10^{-3} respectively, with minimal improvement at higher particle density.

As shown in Table 4, our method achieves excellent volume conservation, with Ours($16\times$) configuration demonstrating 100.00001% (error of 1.26×10^{-7}) and Ours($36\times$)

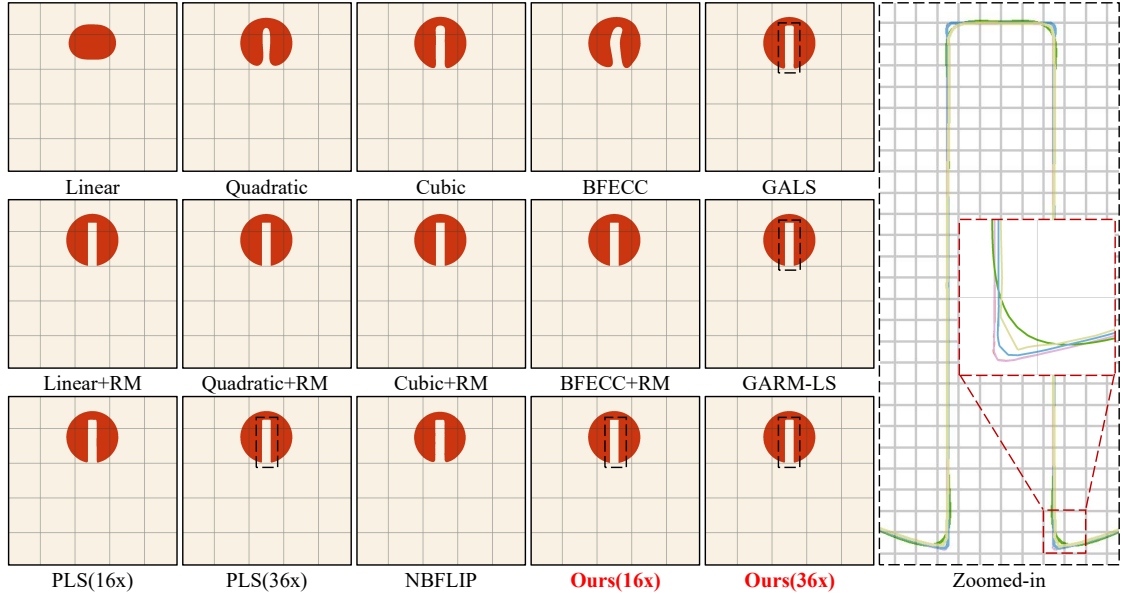


Figure 6: Visual comparison of 200×200 2D Zalesak’s disk interface shapes after one complete revolution across different methods. The zoomed-in view (bottom right) highlights the preservation of sharp corners and edges. First-order methods (Linear) show significant smoothing of corners, while higher-order methods (Quadratic, Cubic) better maintain the overall shape but still round sharp features. Reference map augmentation (bottom row) consistently improves performance. Our method (bottom row, in red) demonstrates superior preservation of geometric features, maintaining sharp corners and straight edges that other methods fail to capture accurately. Zoomed-in view showing GALS (green), PLS (36x) (yellow), Ours (16x) (blue), and Ours (36x) (red).

configuration achieving 99.99999% (error of 1.17×10^{-8}). The exceptional accuracy of our method in this rotation test can be attributed to the particle flow map’s perfect preservation of geometric properties. Since Zalesak’s disk undergoes rigid rotation, our particles maintain their original level set values, gradients, and Hessians without distortion, exactly preserving the interface shape, including sharp corners. This demonstrates the fundamental advantage of our approach: under rigid transformations like rotation, the particle flow map precisely captures the motion without the numerical diffusion inherent in grid-based advection schemes.

Visual inspection of Figure 6 further confirms that our approach preserves the geometric features of the slotted disk with high fidelity, maintaining sharp corners and straight edges that other methods fail to capture accurately. These results demonstrate the effectiveness of our PFM-LS method for applications requiring both precise volume conservation and accurate geometric feature preservation.

Table 4: Relative volume errors for the 200×200 **2D Zalesak’s disk test** after one full revolution ($T = 6.28$ s). All metrics are measured at the final frame.

Method	Volume Preservation (%)	Relative Error
Linear	78.79	2.12×10^{-1}
Linear+RM	100.21	2.10×10^{-3}
Quadratic	100.612	6.13×10^{-3}
Quadratic+RM	99.99	7.70×10^{-5}
Cubic	99.58	4.22×10^{-3}
Cubic+RM	99.99	8.09×10^{-5}
GALS	100.01	1.10×10^{-4}
GARM-LS	99.99	8.18×10^{-5}
PLS(16 \times)	99.24	7.59×10^{-3}
PLS(36 \times)	99.29	7.13×10^{-3}
BFECC	100.89	8.87×10^{-3}
BFECC+RM	99.99	8.95×10^{-5}
NBFLIP	95.29	4.71×10^{-2}
Ours(16\times)	100.00	1.26×10^{-7}
Ours(36\times)	100.00	1.17×10^{-7}

5.2. 2D LeVeque’s Circle

The LeVeque’s circle test provides a challenging scenario for evaluating interface tracking methods under significant deformation. Originally proposed by LeVeque [30], this test has been adapted with modified velocity fields in subsequent studies [41] to create more complex deformations.

In our implementation, we consider a circle with radius $r = 0.15$ centered at $(0.5, 0.5)$ in our $[0, 1]^2$ domain. This circle is deformed by a divergence-free velocity field defined as:

$$\mathbf{u} = u_0 \cos \frac{\pi t}{T} \begin{pmatrix} \cos^2[\pi(x - 0.5)] \sin[2\pi(y - 0.5)] \\ -\sin[2\pi(x - 0.5)] \cos^2[\pi(y - 0.5)] \end{pmatrix}, \quad (27)$$

where $u_0 = 1.0$ and $T = 6.28$ s. At $t = T/2 = 3.14$ s, the circle reaches its maximum deformation, forming a thin filament structure that challenges most interface tracking methods. As the velocity reverses in the second half of the time interval, the shape gradually returns to its initial circular configuration at $t = T = 6.28$ s.

This test is particularly demanding because the circle undergoes severe stretching, creating thin filamentary structures that are difficult to resolve on standard grids. The ability to capture these fine features and recover the original shape upon velocity

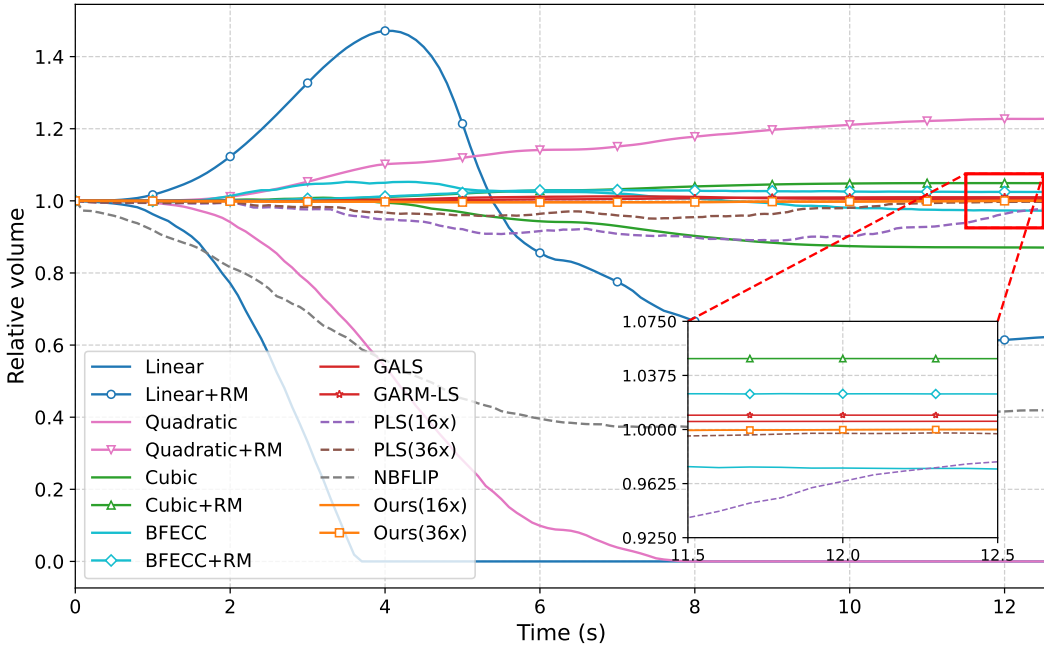


Figure 7: Volume preservation during 200×200 **2D LeVeque’s circle test**. Our method (orange lines) maintains exceptional volume conservation during both maximum deformation ($t = 3.14s$) and recovery phase ($t = 6.28s$). The inset shows detailed performance at the final state, where our method achieves near-perfect recovery ($\approx 100.0\%$), while most other methods exhibit significant volume errors. Lower-order methods like Linear and Quadratic completely lose the interface during extreme deformation.

reversal provides a stringent test of both advection accuracy and feature preservation. We conduct this experiment on a 200×200 simulation grid with various advection algorithms.

Figure 7 presents volume preservation results for LeVeque’s circle test, which poses a more severe challenge than Zalesak’s disk due to extreme deformation creating thin filaments at the midpoint ($t = 6.28s$) before reverting to its original shape. Our proposed narrow-band particle flow map method demonstrates exceptional performance throughout the simulation, maintaining superior volume conservation at both the maximum deformation point and the final state.

Table 5 quantifies the volume preservation at maximum deformation ($t = 6.28s$). The first-order linear scheme struggles significantly, capturing only 0.00% of the initial volume, essentially losing the entire interface. Higher-order methods show progressive improvement, with quadratic and cubic schemes preserving 8.75% and

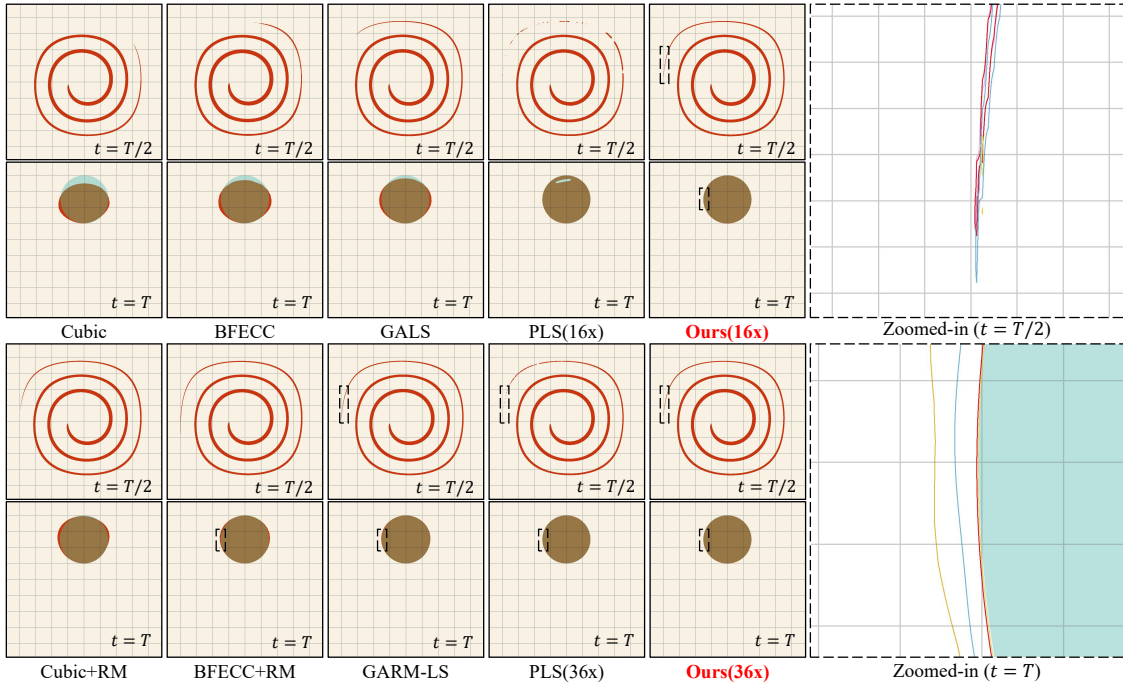


Figure 8: Visual comparison of 200×200 **2D LeVeque's circle test** across different interface-tracking methods. Each panel shows the maximum deformation state (top, $t = T/2$) and the final recovered state (bottom, $t = T$), with the blue outline indicating the ground-truth circle. The zoomed-in views on the right highlight the thin filament structure and recovery accuracy. Zoom-in color legend: PLS (36x), GARM-LS, Ours (16x), Ours (36x).

94.14% respectively. The BFECC method slightly overestimates volume at 102.45%. Reference map augmentation generally improves performance, with Quadratic+RM achieving 114.19% and Cubic+RM yielding 102.91%. Advanced level set methods (GALS and GARM-LS) perform well with GALS at 101.15% and GARM-LS at 100.43%. Particle-based methods show varied results, with PLS(x16) preserving 92.01% and PLS(x36) achieving 96.98%. NBFLIP underperforms at 38.60%.

Our method demonstrates remarkable consistency, with Ours(x16) and Ours(x36) configurations preserving 99.62% and 99.63% respectively at maximum deformation. This near-perfect volume conservation at mid-time is comparable to GARM-LS (100.43%), with both methods achieving near-ideal preservation despite extreme deformation. Our approach's strong performance can be attributed to the particle flow map's ability to accurately track the interface throughout extreme deformation. Unlike other methods that struggle with the thin filamentary structures formed at maximum deformation, our approach maintains precise level set values, gradients,

Table 5: Volume preservation at maximum deformation ($t = 6.28s$) for the 200×200 **2D LeVeque's circle test**

Method	Volume Preservation (%)	Relative Error
Linear	0.00000	1.00000
Quadratic	8.75	9.13×10^{-1}
Cubic	94.14	5.86×10^{-2}
BFECC	102.45	2.45×10^{-2}
Linear+RM	83.49	1.65×10^{-1}
Quadratic+RM	114.20	1.42×10^{-1}
Cubic+RM	102.91	2.91×10^{-2}
BFECC+RM	102.93	2.92×10^{-2}
Hermite(GALS)	101.15	1.15×10^{-2}
Hermite+RM(GARM-LS)	100.43	4.30×10^{-3}
PLS(x16)	92.01	7.99×10^{-2}
PLS(x36)	96.98	3.02×10^{-2}
NBFLIP	38.60	6.14×10^{-1}
Ours(16\times)	99.62	3.80×10^{-3}
Ours(36\times)	99.63	3.75×10^{-3}

and Hessians even in these challenging regions.

At the final time ($t = 12.56s$), when the circle should theoretically return to its initial state, our method demonstrates exceptional recovery capabilities. While most methods show some recovery, with Linear reaching 0.00%, quadratic achieving 87.04%, and cubic at 97.26%, our approach maintains nearly perfect volume preservation with Ours(16 \times) at 100.000022% (2.2×10^{-5} error) and Ours(36 \times) at 99.99998% (2.0×10^{-5} error). Notably, GARM-LS overestimates the volume at 100.99% and performs worse than both GALS (100.57%) and even PLS(x36) (99.69%) in final state recovery. This demonstrates that our method not only handles severe deformation well but also accurately tracks the reversing flow to recover the original shape with unprecedented precision.

The superior performance of our method in this test stems from its ability to maintain high-order interface information through particle trajectories, enabling accurate representation of thin structures during extreme deformation and precise recovery when the flow reverses. This capability sets our approach apart from both traditional grid-based methods and other advanced techniques such as GARM-LS.

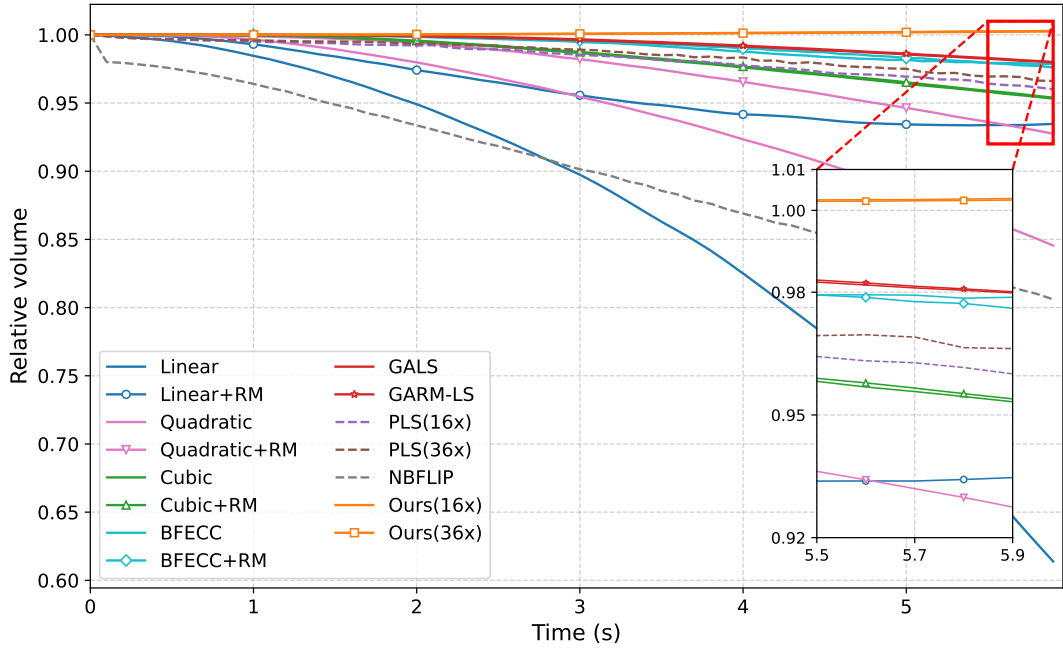


Figure 9: Volume preservation during the 200×200 **2D distorted circle test**. Our method (orange lines) maintains superior volume conservation as the spiral structure develops, achieving 100.3% preservation at final time compared to significant volume loss in other methods. The inset highlights the final stages, where even advanced methods like GALS (97.9%) and GARM-LS (97.9%) lose approximately 2% volume, while traditional methods show more substantial degradation.

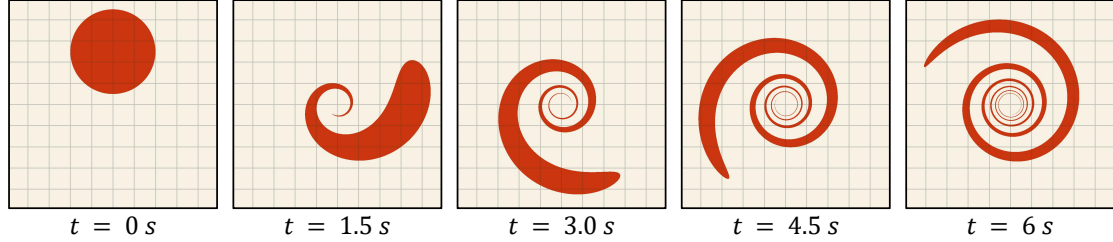


Figure 10: Evolution of the 200×200 **2D distorted circle test** using our method over time. The initially circular interface progressively transforms into a spiral structure due to the differential rotational velocity field, creating increasingly thin filamentary structures that challenge interface tracking methods. Our method preserves these thin structures with high fidelity compared to other approaches.

5.3. 2D Distorted's circle

The distorted circle test presents an extremely challenging case for interface tracking methods, as it creates spiral structures with progressively thinner features. In this

test, a circle with radius $r = 0.2$ centered at $(0.5, 0.5)$ is subjected to a divergence-free rotational velocity field defined as:

$$\mathbf{u} = \frac{u_0}{\sqrt{(x - 0.5)^2 + (y - 0.5)^2 + r_0}}((y - 0.5), -(x - 0.5)) \quad (28)$$

where $u_0 = 0.4$ and $r_0 = 0.01$. This velocity field creates a differential rotation that is stronger near the center and weaker farther away, causing the circle to spiral inward as time progresses.

After $t = 6.0$ seconds, the circle has undergone severe distortion and transforms into a tightly wound spiral. The inner end of the spiral becomes extremely thin, creating sub-grid features that challenge even high-resolution simulations. This test specifically evaluates a method's ability to preserve thin structures and small-scale features that are smaller than the grid resolution. Figure 10 shows the progressive deformation of the interface during the distorted circle test using our method, illustrating how the initially circular shape develops into a thin spiral structure that challenges conventional interface tracking approaches. Even as the spiral becomes increasingly thin, our method maintains excellent interface definition throughout the simulation.

Figure 9 presents volume preservation results across different methods. The distorted circle test reveals dramatic differences in performance, with most methods struggling to maintain even basic volume conservation as the spiral structures become increasingly thin.

Table 6 quantifies the final volume preservation after severe distortion. Traditional methods show significant volume loss, with the linear scheme preserving only 60.01% of the initial volume. Even higher-order methods like quadratic and cubic achieve just 84.05% and 95.20% respectively. Reference map augmentation helps but still falls short, with Linear+RM, Quadratic+RM, and Cubic+RM reaching 93.51%, 92.53%, and 95.27%. Advanced level set methods (GALS and GARM-LS) perform better with 97.91% and 97.94%, but still lose approximately 2% of volume. Particle Level-Set approaches show moderate results, with PLS(x16) and PLS(x36) preserving 95.83% and 96.62%, while NBFLIP maintains only 80.36%.

Most remarkably, our method significantly outperforms all competitors, with Ours(16 \times) and Ours(36 \times) configurations achieving 100.30% and 100.26% volume preservation. While this represents a slight volume gain rather than loss, the magnitude of error remains exceptionally small at approximately 0.3%, dramatically better than all other methods tested. This outstanding performance can be attributed to our particle flow map's ability to maintain high-order information even in regions where spiral structures become extremely thin and fall below grid resolution.

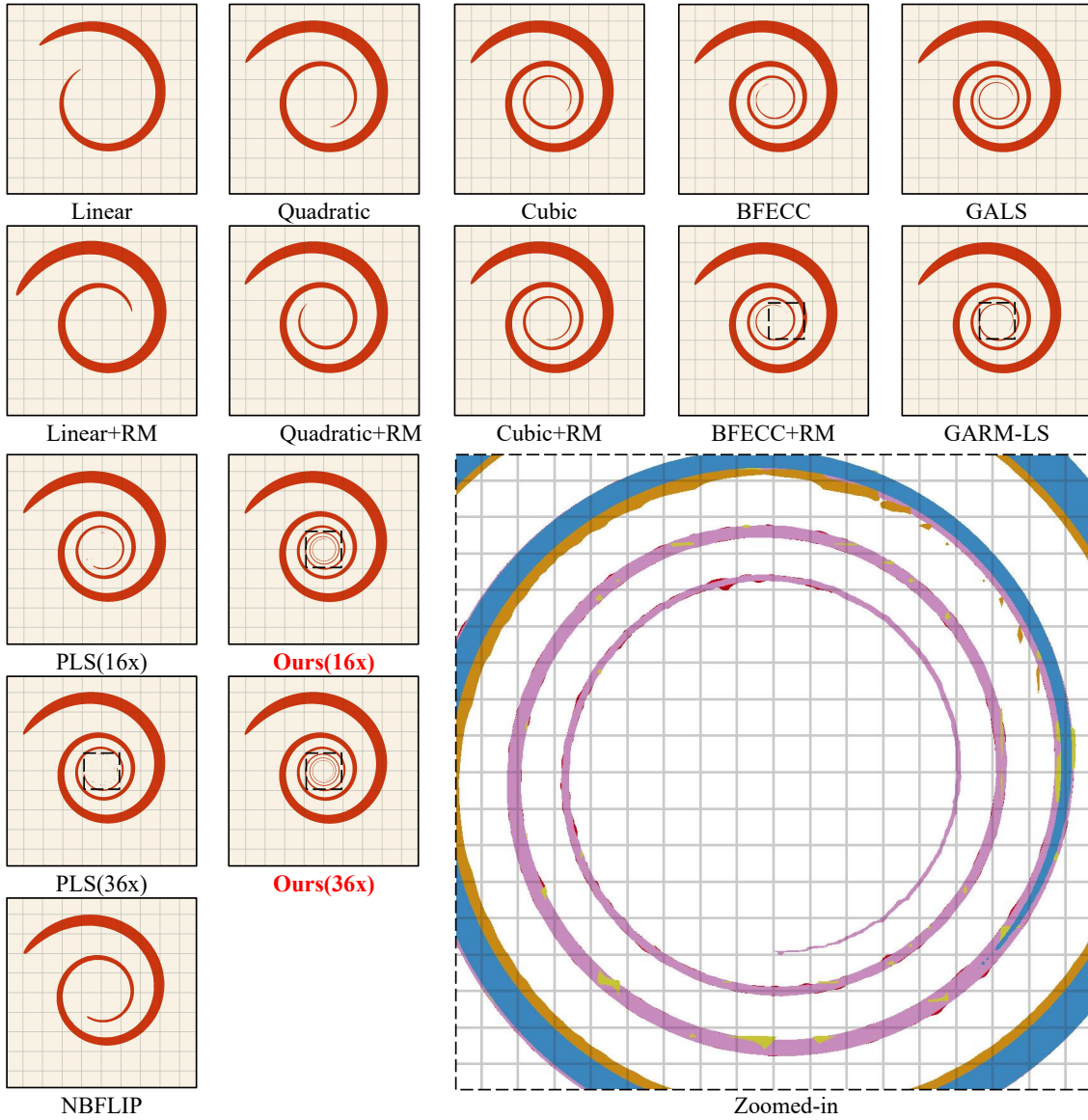


Figure 11: Visual comparison of the 200×200 2D distorted circle test across different interface tracking methods. Lower-order methods (top row) lose significant portions of the spiral structure, while higher-order and reference map methods (middle rows) preserve more but still lose inner details. Our method (highlighted in red) preserves the complete spiral structure with exceptional fidelity, maintaining continuous thin features even where they become extremely thin. The zoomed-in view (right) reveals our method’s superior ability to capture sub-grid features that other methods fail to represent. Zoomin Method color: BFECC+RM, PLS (36 \times), GARM-LS, Ours (16 \times), Ours (36 \times),

Table 6: Volume preservation for the 200×200 **2D distorted circle test** at final time

Method	Volume Preservation (%)	Relative Error
Linear	60.01	4.00×10^{-1}
Quadratic	84.05	1.60×10^{-1}
Cubic	95.20	4.80×10^{-2}
BFECC	97.81	2.19×10^{-2}
Linear+RM	93.51	6.49×10^{-2}
Quadratic+RM	92.53	7.47×10^{-2}
Cubic+RM	95.27	4.73×10^{-2}
BFECC+RM	97.54	2.46×10^{-2}
Hermite(GALS)	97.91	2.09×10^{-2}
Hermite+RM(GARM-LS)	97.94	2.06×10^{-2}
PLS(x16)	95.83	4.17×10^{-2}
PLS(x36)	96.62	3.38×10^{-2}
NBFLIP	80.36	1.96×10^{-1}
Ours(x16)	100.30	3.00×10^{-3}
Ours(x36)	100.26	2.60×10^{-3}

Visual inspection of Figure 11 further confirms the superiority of our approach. While other methods lose the thin spiral tails once they become sub-grid features, our method preserves these fine structures with high fidelity. The particle flow map accurately tracks the interface as it evolves into complex geometries, maintaining both the global shape and intricate details that competing methods fail to capture.

This challenging test highlights the strength of the narrow-band particle flow map framework for simulations involving extreme deformation and sub-grid features. By leveraging the high-order information carried by particles and the precise motion tracking of flow maps, our method faithfully represents thin structures even under conditions that defeat conventional grid-based and particle schemes.

5.4. 3D LeVeque’s Circle

Following our 2D experiments, we extend our evaluation to challenging 3D scenarios to assess how our method handles volume preservation in higher dimensions. Our first 3D test implements a spherical version of the LeVeque’s circle, subjecting a sphere to severe stretching and compression before returning it to its original shape, following the methodology in [41].

In our implementation, a sphere with radius $r = 0.15$ is initially centered at $(0.35, 0.35, 0.35)$ within our $[0, 1]^3$ domain. This sphere is deformed by a divergence-free velocity field $\mathbf{u} = (u, v, w)$ defined as:

$$\begin{cases} u = 2u_0 \cos \frac{\pi t}{T} \cos^2[2\pi(x - 0.5)] \sin[2\pi(y - 0.5)] \sin[2\pi(z - 0.5)], \\ v = -u_0 \cos \frac{\pi t}{T} \sin[2\pi(x - 0.5)] \cos^2[2\pi(y - 0.5)] \sin[2\pi(z - 0.5)], \\ w = -u_0 \cos \frac{\pi t}{T} \sin[2\pi(x - 0.5)] \sin[2\pi(y - 0.5)] \cos^2[2\pi(z - 0.5)], \end{cases} \quad (29)$$

where $u_0 = 0.25$ m/s and $T = 10.0$ s. Under this velocity field, the sphere undergoes maximum deformation at $t = T/2 = 5.0$ seconds, developing into a complex folded structure with thin features. The velocity then reverses direction, theoretically returning the sphere to its original shape at $t = T = 10.0$ seconds.

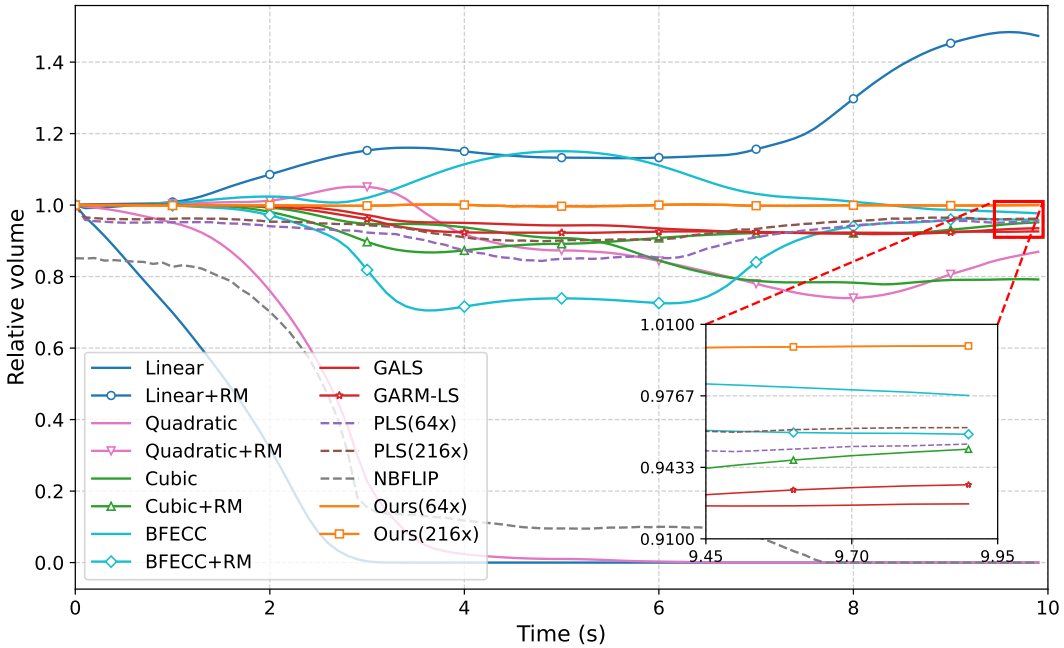


Figure 12: Volume preservation comparison during the 50^3 **3D LeVeque sphere test**. Our method (orange lines) maintains nearly perfect volume conservation throughout the simulation, including both the deformation phase (0-5s) and the recovery phase (5-10s). The inset shows detailed performance during the critical recovery phase, where our method achieves over 99.9% volume preservation while other methods exhibit significant volume loss or inaccurate volume gain. Linear and quadratic methods completely lose the interface, while most advanced methods struggle to maintain accurate volume during the complex 3D deformation and reversal.

We conduct these experiments on a 50^3 grid and compare the volume preservation capabilities of various methods throughout the deformation and recovery process.

For particle-based methods, we use $4 \times 4 \times 4 = 64$ particles (4 particles along each axis) for the lower density configurations (PLS(x64), ours(x64)) and $6 \times 6 \times 6 = 216$ particles for the higher density configurations (PLS(x216), ours(x216)). The results demonstrate how different approaches handle the challenges of extreme 3D deformation.

Figure 12 presents volume preservation results for the 3D LeVeque’s sphere test. The three-dimensional case introduces substantially greater challenges than its 2D counterpart, with most methods struggling to maintain volume under extreme deformation. Table 7 quantifies volume preservation at maximum deformation ($t = 5.0$ s). The results reveal dramatic performance differences across methods. Lower-order methods show significant volume loss: the first-order linear scheme completely fails (0.00% preservation), while the quadratic scheme preserves just 1.01%. Even the cubic scheme preserves only 90.78% of the initial volume. Grid-based methods with reference map augmentation show inconsistent results—Linear+RM overestimates at 113.27%, while Quadratic+RM and Cubic+RM preserve 87.31% and 89.18%, respectively. Advanced level set approaches GALS and GARM-LS perform better with 94.31% and 92.28% preservation. Particle-based methods show moderate success, with PLS(x64) and PLS(x216) preserving 84.86% and 90.14%, while NBFLIP struggles severely at just 9.55%.

Our narrow band PFM-LS method substantially outperforms all competitors at maximum deformation, with both Ours(64 \times) and Ours(216 \times) configurations achieving 99.68% volume preservation. This near-perfect conservation under extreme 3D deformation demonstrates our approach’s exceptional capability to track complex interfaces in three dimensions.

Performance differences become even more pronounced at the final time ($t = 10.0$ s), when the sphere should theoretically return to its original shape. The linear and quadratic schemes completely lose the interface (0.00% preservation), while the cubic scheme recovers only 79.09%. Reference map methods show highly variable results—Linear+RM significantly overestimates at 146.65%, while Quadratic+RM and Cubic+RM achieve 87.25% and 95.32%. GALS and GARM-LS perform moderately with 92.61% and 93.56%, demonstrating that even advanced level set methods struggle with flow reversal in 3D.

Particle-based methods generally show advantages in this reversal scenario. PLS(x64) and PLS(x216) recover 95.44% and 96.33% of the original volume, indicating that particle methods typically capture reversing flows better than pure grid-based approaches. NBFLIP, however, fails completely with 0.00% recovery. Most remarkably, our method achieves nearly perfect recovery, with Ours(64 \times) and Ours(216 \times) configurations preserving 99.97% and 99.99% of the original volume, respectively. This

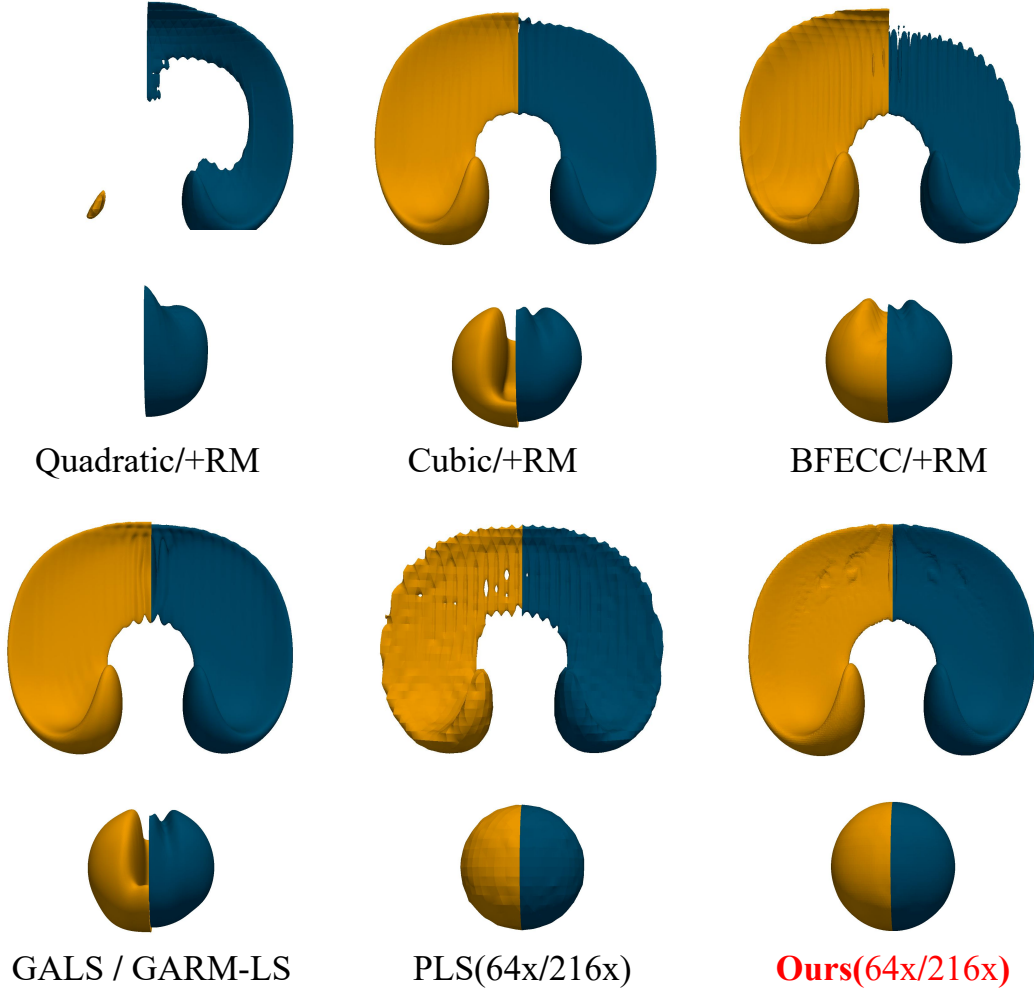


Figure 13: Visual comparison of 50^3 **3D LeVeque sphere test** results across different interface tracking methods. Each panel shows maximum deformation state (top) and final recovered state (bottom). The two-color visualization (gold/blue) in each panel compares method pairs: Quadratic without/with Reference Map, Cubic without/with Reference Map, BFECC without/with Reference Map, GALS/GARM-LS, and PLS with different particle densities (64x/216x). Our method (shown in red) is displayed with both 64x and 216x particle configurations. This comparative visualization reveals that while Reference Map augmentation generally improves performance for traditional methods, our approach delivers superior shape preservation and nearly perfect recovery regardless of particle density, outperforming all competing methods in this challenging 3D deformation test.

extraordinary accuracy in both deformation and reversal phases highlights the fundamental advantage of our particle flow map approach: by tracking interface points with high-order information through accurate trajectories, we faithfully capture even the most complex 3D deformations and recoveries.

The 3D LeVeque test results clearly demonstrate that three-dimensional interface tracking presents substantially greater challenges than 2D scenarios. Many methods that perform adequately in 2D struggle in 3D, particularly during the reversal phase. Our method’s consistent excellence across both 2D and 3D tests, and in both deformation and reversal phases, confirms its robustness and superiority for complex interface tracking applications.

Table 7: Volume preservation at maximum deformation ($t = 5.0$ s) for the 50^3 **3D LeVeque’s sphere test**

Method	Volume Preservation (%)	Relative Error
Linear	0.00%	1.00000
Quadratic	1.01%	9.90×10^{-1}
Cubic	90.78%	9.22×10^{-2}
BFECC	115.06%	1.51×10^{-1}
Linear+RM	113.27%	1.33×10^{-1}
Quadratic+RM	87.31%	1.27×10^{-1}
Cubic+RM	89.18%	1.08×10^{-1}
BFECC+RM	73.90%	2.61×10^{-1}
Hermite(GALS)	94.31%	5.69×10^{-2}
Hermite+RM(GARM-LS)	92.28%	7.72×10^{-2}
PLS(x64)	84.86%	1.51×10^{-1}
PLS(x216)	90.14%	9.86×10^{-2}
NBFLIP	9.55%	9.04×10^{-1}
Ours(64\times)	99.68%	3.16×10^{-3}
Ours(216\times)	99.68%	3.16×10^{-3}

5.5. 3D Distorted Sphere

Building upon our previous 3D evaluation, we now examine another demanding scenario by extending the 2D distorted circle test into three dimensions. This 3D distorted sphere test represents one of the most challenging benchmarks for interface tracking methods, as it generates complex spiral structures with progressively thinner features that evolve in three-dimensional space.

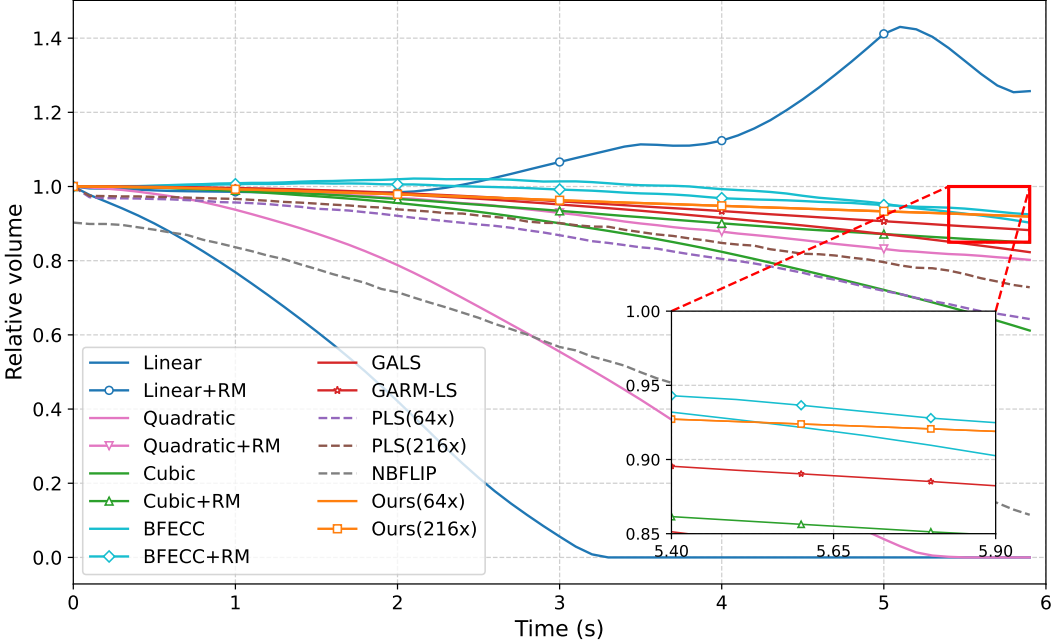


Figure 14: Volume preservation comparison during the 50^3 **3D distorted sphere test**. Our method (orange lines) maintains good volume preservation throughout the simulation. Although BFECC+RM shows slightly better final volume preservation, it erroneously increases volume around 2.5s (visible in the inset), while our method exhibits only physically consistent volume loss. Most other methods suffer from significant volume deterioration as the spiral structure develops.

In our implementation, a sphere with radius $r = 0.2$ is initially centered at $(0.5, 0.75, 0.5)$ within our $[0, 1]^3$ domain. The sphere is subjected to a rotational velocity field defined as:

$$\mathbf{u} = \frac{u_0}{\sqrt{(x - 0.5)^2 + (y - 0.5)^2 + r_0^2}}((y - 0.5), -(x - 0.5), 0) \quad (30)$$

where $u_0 = 0.4$ m/s and $r_0 = 0.01$ m. This velocity field creates a differential rotation in the xy-plane that is stronger near the center axis and weaker farther away, causing the sphere to spiral inward as time progresses.

From $t = 0$ to $t = 6.0$ seconds, the sphere undergoes severe distortion and transforms into a complex spiral structure. The inner regions of the spiral become extremely thin, creating sub-grid features that challenge even high-resolution simulations. This test specifically evaluates a method's ability to preserve thin structures and small-scale features in three dimensions that may be smaller than the grid resolution.

We conduct these experiments on a 50^3 grid, consistent with our 3D LeVeque’s sphere test setup. As in the previous experiment, we use $4 \times 4 \times 4 = 64$ particles per cell for the lower density configurations (PLS(x64), Ours(64 \times)) and $6 \times 6 \times 6 = 216$ particles per cell for the higher density configurations (PLS(x216), Ours(216 \times)).

Figure 14 illustrates the performance of various methods in this highly challenging test, with quantitative results presented in Table 8. Table 8 quantifies the volume preservation at the final simulation time. The results reveal significant performance differences across methods. Lower-order schemes struggle severely, with both linear and quadratic methods completely failing to preserve any volume (0.00%). Even the cubic scheme maintains only 60.08% of the original volume. Grid-based methods with reference map augmentation show mixed behavior—Linear+RM significantly overestimates at 126.89%, while Quadratic+RM and Cubic+RM preserve 79.96% and 84.76%, respectively. The advanced level set methods GALS and GARM-LS achieve moderate preservation with 81.79% and 88.01%, but still lose substantial volume under this extreme deformation.

Particle-based methods demonstrate varied performance. Traditional particle level set approaches struggle considerably, with PLS(x64) and PLS(x216) configurations preserving only 63.67% and 72.70% of the original volume. NBFLIP shows poor results with just 10.27% preservation, confirming its limitations in handling complex 3D structures.

Our PFM-LS approach delivers significantly better performance, with both Ours(64 \times) and Ours(216 \times) configurations achieving approximately 91.72% volume preservation. While BFECC+RM slightly outperforms our method at 92.28%, analysis of the volume preservation curve in Figure 14 reveals an important distinction: BFECC+RM erroneously increases the volume during advection, reaching a peak of 100.89% before decreasing to its final value. In contrast, our method only experiences volume loss throughout the simulation without any erroneous volume increase.

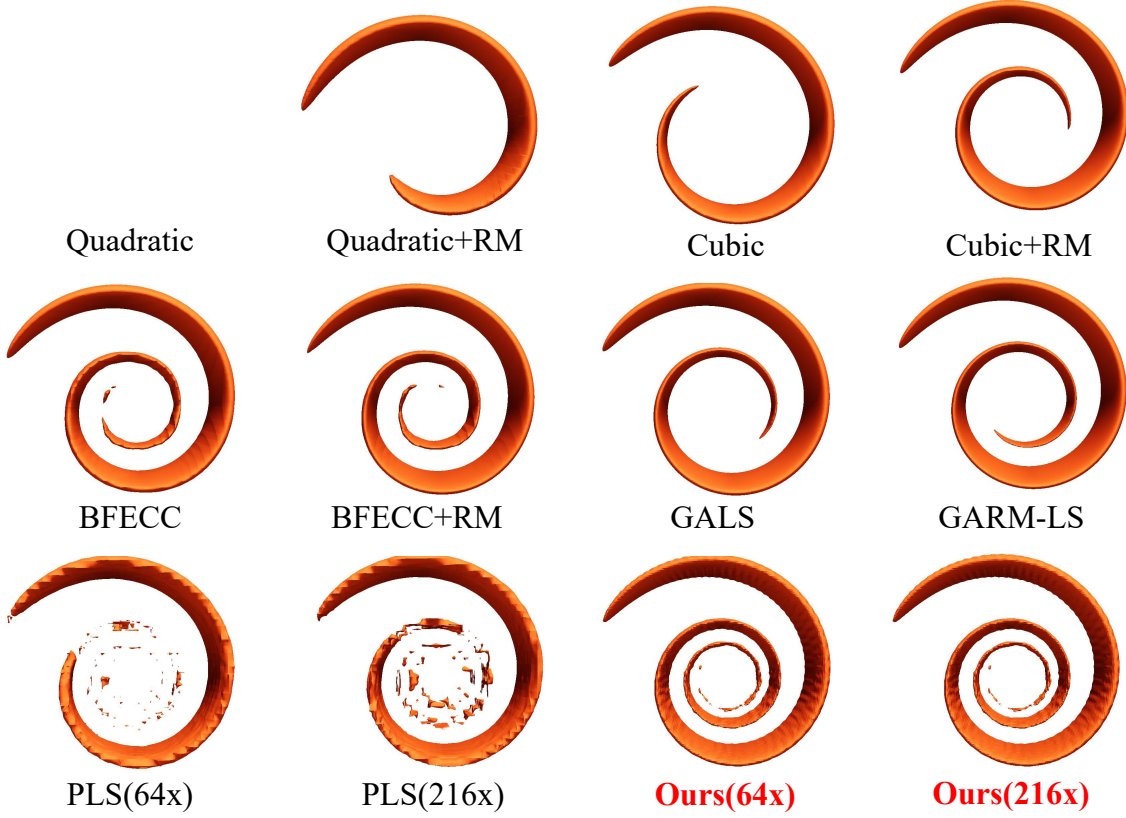


Figure 15: Visual comparison of the 50^3 **3D distorted sphere** test results across different interface tracking methods after 6.0 seconds of differential rotation. Each method demonstrates varying abilities to preserve the evolving spiral structure. Lower-order methods (Quadratic, Quadratic+RM) capture only outer portions of the spiral. Higher-order methods (Cubic, Cubic+RM, BFECC, BFECC+RM) preserve more of the structure but still lose inner details. Advanced level set methods (GALS, GARM-LS) maintain better continuity but exhibit some distortion. Traditional particle-based methods (PLS with $64\times$ and $216\times$ particles) suffer from significant discontinuities in the inner spiral. In contrast, our method (shown in red) preserves the complete spiral structure with superior fidelity, maintaining continuous thin features and clear boundaries even in regions where the spiral becomes extremely thin, demonstrating the effectiveness of our narrow band particle flow map approach for capturing sub-grid features.

Visual comparison in Figure 15 further validates our method’s advantages. Despite the similar final volume preservation percentages between our approach and BFECC+RM, our method captures the fine spiral tail structures with significantly greater fidelity. These thin features, which fall below grid resolution in the most

Table 8: Volume preservation for the 50^3 **3D distorted sphere test** at final time

Method	Volume Preservation (%)	Relative Error
Linear	0.00%	1.00
Quadratic	0.00%	1.00
Cubic	60.08%	3.99×10^{-1}
BFECC	89.66%	1.03×10^{-1}
Linear+RM	126.89%	2.70×10^{-1}
Quadratic+RM	79.96%	2.00×10^{-1}
Cubic+RM	84.76%	1.52×10^{-1}
BFECC+RM	92.28%	7.72 $\times 10^{-2}$
Hermite(GALS)	81.79%	1.82×10^{-1}
Hermite+RM(GARM-LS)	88.01%	1.20×10^{-1}
PLS(x64)	63.67%	3.63×10^{-1}
PLS(x216)	72.70%	2.73×10^{-1}
NBFLIP	10.27%	8.97×10^{-1}
Ours(64\times)	91.72%	8.28 $\times 10^{-2}$
Ours(216\times)	91.72%	8.28 $\times 10^{-2}$

challenging regions, are preserved with remarkable clarity in our simulations while appearing diffused or disconnected in other methods.

The 3D distorted sphere test demonstrates that tracking complex spiral structures in three dimensions presents extreme challenges for interface methods. The fact that our approach maintains over 91% volume preservation while accurately representing sub-grid features underscores the effectiveness of our narrow band particle flow map for handling the most demanding interface tracking scenarios.

5.6. Redistance

In this section, we evaluate the performance of our particle Newton redistance method and compare it with two established approaches—the Hermite Fast Marching Method (HFMM) and Hermite Newton (HNewton) from Li et al. [31]. Redistancing frequency plays a critical role in level-set methods: more frequent redistancing (corresponding to smaller “steps” values in our tests) better preserves the signed-distance property but can introduce interface distortion. We conduct our evaluation using the 200×200 LeVeque’s circle test, which provides a standard benchmark for assessing redistancing accuracy and interface stability.

Figure 16 presents a comparative analysis of relative volume errors for each method across different redistancing frequencies. Lower steps indicate more frequent

redistancing, which is particularly relevant for applications like liquid simulation where redistancing occurs often to maintain numerical stability.

At high redistancing frequency (6 steps), HFMM shows significant volume distortion with errors exceeding 12% at maximum deformation and approximately 4% in the final state. Hermite Newton performs better but still exhibits errors of approximately 3.5% at maximum deformation. In contrast, our method maintains excellent volume preservation with errors below 1% regardless of redistancing frequency, demonstrating remarkable insensitivity to this parameter.

As redistancing becomes less frequent (increasing to 50 steps), HFMM and HNewton show improved volume preservation, though still not matching our method’s consistency. This insensitivity to redistancing frequency represents a significant advantage of our approach, as it allows for flexible redistancing schedules without compromising accuracy.

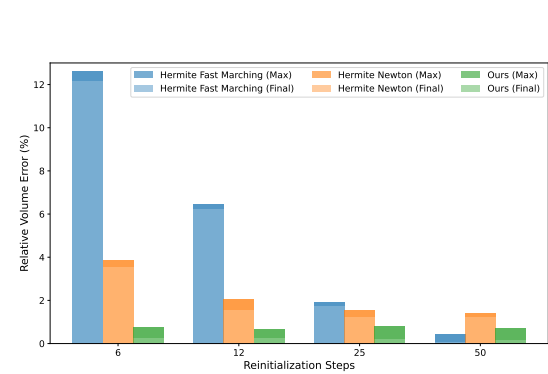


Figure 16: Relative volume error comparison of different **redistancing methods** in the 200×200 2D LeVeque’s circle test across varying redistancing frequencies (6, 12, 25, and 50 steps). Lower step values indicate more frequent redistancing. Our method (green) maintains consistently low error across all frequencies, whereas Hermite Fast Marching (blue) and Hermite Newton (orange) exhibit higher sensitivity to redistancing frequency.

The quantitative data reveals that our method preserves between 99.21% and 99.82% of the original volume across all tested frequencies. Even with the most aggressive redistancing (6 steps), our approach achieves 99.29% volume preservation at maximum deformation and 99.72% at the final state, demonstrating exceptional stability.

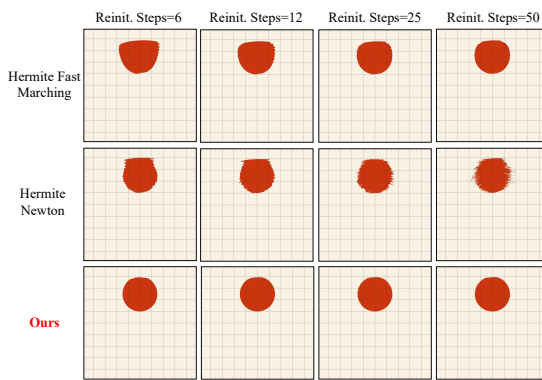


Figure 17: **Redistancing test.** Visual comparison of interface shapes after redistancing using different methods and frequencies. Top, middle, and bottom rows correspond to Hermite Fast Marching, Hermite Newton, and our method. Columns represent redistancing frequencies of 6, 12, 25, and 50 steps. Our method preserves the circular interface across all frequencies, whereas others exhibit noticeable distortions.

Figure 17 provides visual confirmation of these numerical findings. The ideal outcome of redistancing should maintain the original circular shape without introducing artifacts. Our method consistently preserves the circle’s shape across all frequencies, with virtually no visible difference between 6 steps and 50 steps. This indicates that our approach maintains geometric fidelity regardless of how frequently redistancing occurs. In contrast, HFMM exhibits significant shape distortion at high redistancing frequencies, with the interface appearing flattened and irregular, progressively improving as redistancing becomes less frequent. Hermite Newton shows better shape preservation than HFMM but still develops noticeable artifacts at various frequencies, particularly evident in the 50 steps case where small perturbations appear along the interface.

The visual results clearly demonstrate our method’s ability to maintain the original circular interface shape regardless of redistancing frequency. This consistency is crucial for applications like liquid simulation where frequent redistancing is necessary, as our approach allows for aggressive redistancing schedules without compromising interface fidelity. This superior redistancing performance stems from our hybrid particle-grid blending approach described in Section 4.3. By intelligently combining particle information near the interface with redistributed grid values elsewhere, our method effectively maintains both the signed distance property and high-order geometric information captured by particles.

These results confirm that our particle Newton redistance method offers the best combination of shape preservation and insensitivity to redistancing frequency among the tested approaches, making it particularly well-suited for applications requiring frequent redistancing while maintaining precise interface geometries.

5.7. Convergence Analysis

To evaluate the numerical convergence of our method compared to existing approaches, we conducted **convergence test** on 200×200 2D distorted circle benchmark cases introduced in Sections 5.3, respectively. For these tests, we performed short-duration simulations (30 time steps, equivalent to 0.6s) to focus specifically on the numerical order of convergence rather than long-term behavior.

We analyzed convergence by computing the error between numerical solutions at different grid resolutions and fitting these errors to a power law using least squares regression. The quality of the fit is measured by the coefficient of determination (R^2), with values closer to 1.0 indicating more consistent convergence behavior.

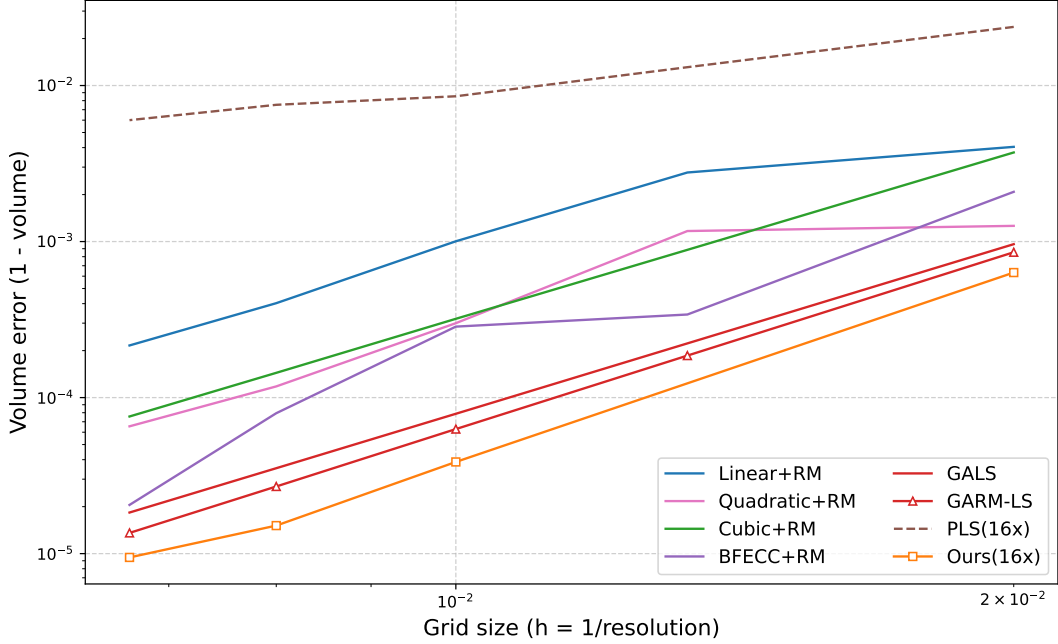


Figure 18: **Convergence analysis** for the 200×200 2D distorted circle test, comparing error reduction across grid refinements for different interface tracking methods. Our method achieves nearly fourth-order convergence.

In 200×200 2D distorted circle test, as illustrated in Figure 18, our method maintained superior performance with a convergence rate of 3.9084 ($R^2 = 0.9969$), again approaching fourth-order accuracy. Other high-performing methods included BFECC+RM with 3.8600 ($R^2 = 0.9391$), GARM-LS with 3.7715 ($R^2 = 1.0000$), and GALS with 3.6058 ($R^2 = 1.0000$). Cubic+RM achieved 3.5474 ($R^2 = 1.0000$), while lower-order methods showed improved but still inferior rates: Quadratic+RM at 2.9074 ($R^2 = 0.8990$) and Linear+RM at 2.7744 ($R^2 = 0.9390$). PLS(x16) exhibited first-order convergence at 1.2430 ($R^2 = 0.9833$).

Our method achieves nearly fourth-order convergence in the test case due to its integration of particle flow maps with high-order information. Combined with the volume preservation results from previous sections, these findings demonstrate our approach’s suitability for precise interface tracking applications.

6. Conclusion

In this work, we presented PFM-LS, a particle flow map method for high-fidelity level-set interface tracking. The method incorporates bidirectional flow maps to

advect particle-embedded level set values, gradients, and Hessians. By integrating redistancing and resampling within a narrow band structure, the method achieves accurate interface reconstruction while maintaining computational efficiency.

Our method bridges several lines of prior work. Compared to Particle Level Set [12], which uses particles primarily for error correction, PFM-LS employs particles as primary carriers of geometric information, achieving significantly better volume preservation (10^{-7} vs. 10^{-3} relative error). Compared to GALS [42] and GARM-LS [31], our particle-based formulation naturally captures sub-grid features without grid-based interpolation errors. Among particle flow map methods [75, 40, 11], PFM-LS is the first to apply this framework to level set interface tracking, extending the differential forms perspective from impulse and vorticity to interface geometry. The results from 2D and 3D benchmark tests demonstrate that PFM-LS delivers competitive performance compared to established methods in terms of geometric fidelity, volume conservation, and the preservation of fine-scale structures. Notably, the solver effectively handles complex interface deformations, including high-curvature features, without excessive particle clustering or loss of resolution.

Limitations and Future Work... Several limitations warrant further investigation. First, while adaptive particle control maintains coverage in most scenarios, particles near fine-scale features such as thin filaments or high-curvature regions may disperse during advection, causing the method to fall back to the less accurate background grid representation. More refined adaptive control that accounts for local interface complexity is needed to address this issue. Second, the current topological change detection relies on gradient consistency thresholds; overly aggressive settings may erroneously merge nearby interfaces or smooth out fine details, while conservative settings may fail to detect legitimate topology changes. Developing robust, geometry-aware detection mechanisms remains an open challenge. Finally, per-particle Jacobian storage incurs higher memory overhead than purely grid-based methods, which may become a concern for large-scale 3D simulations.

In conclusion, the PFM-LS framework provides an efficient and accurate approach for level-set interface tracking. Future work will extend this framework to applications involving surface tension, multiphase flows, liquid simulations, fire dynamics, and differentiable fluid simulators with free surfaces, where precise and stable interface handling remains essential.

7. Acknowledgment

Georgia Tech authors acknowledge NSF IIS #2433322, ECCS #2318814, CAREER #2433307, IIS #2106733, OISE #2433313, CNS #2450401, and CNS #1919647

for funding support.

References

- [1] David Adalsteinsson and James A Sethian. A fast level set method for propagating interfaces. *Journal of computational physics*, 118(2):269–277, 1995.
- [2] Lakshman Anumolu and Mario F Trujillo. Gradient augmented level set method for phase change simulations. *Journal of Computational Physics*, 353:377–406, 2018.
- [3] Adam W Bargteil, Tolga G Goktekin, James F O’brien, and John A Strain. A semi-lagrangian contouring method for fluid simulation. *ACM Transactions on Graphics (TOG)*, 25(1):19–38, 2006.
- [4] Arne Böckmann and Magnus Vartdal. A gradient augmented level set method for unstructured grids. *Journal of Computational Physics*, 258:47–72, 2014.
- [5] Duowen Chen, Zhiqi Li, Junwei Zhou, Fan Feng, Tao Du, and Bo Zhu. Solid-fluid interaction on particle flow maps. *ACM Transactions on Graphics (TOG)*, 43(6):1–20, 2024.
- [6] Duowen Chen, Zhiqi Li, Taiyuan Zhang, Jinjin He, Junwei Zhou, Bart G van Bloemen Waanders, and Bo Zhu. Fluid simulation on compressible flow maps. *ACM Transactions on Graphics (TOG)*, 44(4):1–17, 2025.
- [7] Duowen Chen, Junwei Zhou, and Bo Zhu. A neural particle level set method for dynamic interface tracking. *ACM Transactions on Graphics*, 44(3):1–21, 2025.
- [8] Nuttapong Chentanez and Matthias Müller. Mass-conserving eulerian liquid simulation. *IEEE Transactions on Visualization and Computer Graphics*, 20(1):17–29, 2013.
- [9] Ricardo Cortez. *Impulse-based particle methods for fluid flow*. University of California, Berkeley, 1995.
- [10] Georges-Henri Cottet, Emmanuel Maitre, and Thomas Milcent. Eulerian formulation and level set models for incompressible fluid-structure interaction. *ESAIM: Mathematical Modelling and Numerical Analysis*, 42(3):471–492, 2008.
- [11] Yitong Deng, Hong-Xing Yu, Diyang Zhang, Jiajun Wu, and Bo Zhu. Fluid simulation on neural flow maps. *ACM Trans. Graph.*, 42(6), 2023.

- [12] Douglas Enright, Ronald Fedkiw, Joel Ferziger, and Ian Mitchell. A hybrid particle level set method for improved interface capturing. *Journal of Computational physics*, 183(1):83–116, 2002.
- [13] Ronald Fedkiw, Jos Stam, and Henrik Wann Jensen. Visual simulation of smoke. In *Proceedings of the 28th annual conference on Computer graphics and interactive techniques*, pages 15–22, 2001.
- [14] Fan Feng, Jinyuan Liu, Shiying Xiong, Shuqi Yang, Yaorui Zhang, and Bo Zhu. Impulse fluid simulation. *IEEE Transactions on Visualization and Computer Graphics*, 29(6):3081–3092, 2022.
- [15] Florian Ferstl, Ryoichi Ando, Chris Wojtan, Rüdiger Westermann, and Nils Thuerey. Narrow band flip for liquid simulations. In *Computer Graphics Forum*, volume 35, pages 225–232. Wiley Online Library, 2016.
- [16] Zheng Fu, Shi-Yu Wu, and Kai-Xin Liu. Gradient-augmented hybrid interface capturing method for incompressible two-phase flow. *Chinese Physics B*, 25(6):064701, 2016.
- [17] Frederic Gibou, Ronald Fedkiw, and Stanley Osher. A review of level-set methods and some recent applications. *Journal of Computational Physics*, 353:82–109, 2018.
- [18] Frederic Gibou, David Hyde, and Ron Fedkiw. Sharp interface approaches and deep learning techniques for multiphase flows. *Journal of Computational Physics*, 380:442–463, 2019.
- [19] Oscar Gonzalez and A. M. Stuart. *A first course in continuum mechanics*. Cambridge texts in applied mathematics ; 42. Cambridge University Press, Cambridge, 2008. ISBN 1-107-18691-9.
- [20] Jinjin He, Taiyuan Zhang, Hiroki Kobayashi, Atsushi Kawamoto, Yuqing Zhou, Tsuyoshi Nomura, and Bo Zhu. Multi-level partition of unity on differentiable moving particles. *ACM Transactions on Graphics (TOG)*, 43(6):1–21, 2024.
- [21] Nambin Heo and Hyeong-Seok Ko. Detail-preserving fully-eulerian interface tracking framework. *ACM Trans. Graph.*, 29(6):176, 2010.
- [22] Simone E Hieber and Petros Koumoutsakos. A lagrangian particle level set method. *Journal of Computational Physics*, 210(1):342–367, 2005.

- [23] Sandro Ianniello and Andrea Di Mascio. A self-adaptive oriented particles level-set method for tracking interfaces. *Journal of Computational Physics*, 229(4):1353–1380, 2010.
- [24] Chenfanfu Jiang, Craig Schroeder, Andrew Selle, Joseph Teran, and Alexey Stomakhin. The affine particle-in-cell method. *ACM Transactions on Graphics (TOG)*, 34(4):1–10, 2015.
- [25] Guang-Shan Jiang and Danping Peng. Weighted eno schemes for hamilton–jacobi equations. *SIAM Journal on Scientific computing*, 21(6):2126–2143, 2000.
- [26] Ebrahim M Kolahdouz and David Salac. A semi-implicit gradient augmented level set method. *SIAM Journal on Scientific Computing*, 35(1):A231–A254, 2013.
- [27] Dmitry Kolomenskiy, Jean-Christophe Nave, and Kai Schneider. Adaptive gradient-augmented level set method with multiresolution error estimation. *Journal of Scientific Computing*, 66:116–140, 2016.
- [28] Michael Lentine, Matthew Cong, Saket Patkar, and Ronald Fedkiw. Simulating free surface flow with very large time steps. In *Proceedings of the 11th ACM SIGGRAPH/Eurographics conference on Computer Animation*, pages 107–116, 2012.
- [29] Shingyu Leung and Hongkai Zhao. A grid based particle method for moving interface problems. *Journal of Computational Physics*, 228(8):2993–3024, 2009.
- [30] Randall J Leveque. High-resolution conservative algorithms for advection in incompressible flow. *SIAM Journal on Numerical Analysis*, 33(2):627–665, 1996.
- [31] Xingqiao Li, Xingyu Ni, Bo Zhu, Bin Wang, and Baoquan Chen. Garm-ls: A gradient-augmented reference-map method for level-set fluid simulation. *ACM Transactions on Graphics (TOG)*, 42(6):1–20, 2023.
- [32] Zhiqi Li, Duowen Chen, Candong Lin, Jinyuan Liu, and Bo Zhu. Particle-laden fluid on flow maps. *arXiv preprint arXiv:2409.06246*, 2024.
- [33] Zhiqi Li, Jinjin He, Barnabás Börcsök, Taiyuan Zhang, Duowen Chen, Tao Du, Ming C Lin, Greg Turk, and Bo Zhu. An adjoint method for differentiable fluid simulation on flow maps. *arXiv preprint arXiv:2511.01259*, 2025.

[34] Zhiqi Li, Candong Lin, Duowen Chen, Xinyi Zhou, Shiying Xiong, and Bo Zhu. Clebsch gauge fluid on particle flow maps. *ACM Transactions on Graphics (TOG)*, 44(4):1–12, 2025.

[35] Zhiqi Li, Ruicheng Wang, Junlin Li, Duowen Chen, Sinan Wang, and Bo Zhu. Edge: Epsilon-difference gradient evolution for buffer-free flow maps. *ACM Transactions on Graphics (TOG)*, 44(4):1–11, 2025.

[36] Xu-Dong Liu, Stanley Osher, and Tony Chan. Weighted essentially non-oscillatory schemes. *Journal of computational physics*, 115(1):200–212, 1994.

[37] Konstantinos G Lyras, Bruce Hanson, Michael Fairweather, and Peter J Heggs. A coupled level set and volume of fluid method with a re-initialisation step suitable for unstructured meshes. *Journal of Computational Physics*, 407:109224, 2020.

[38] Olivier Mercier. Numerical methods for set transport and related partial differential equations. 2013.

[39] Olivier Mercier, Xi-Yuan Yin, and Jean-Christophe Nave. The characteristic mapping method for the linear advection of arbitrary sets. *SIAM Journal on Scientific Computing*, 42(3):A1663–A1685, 2020.

[40] Mohammad Sina Nabizadeh, Stephanie Wang, Ravi Ramamoorthi, and Albert Chern. Covector fluids. *ACM Transactions on Graphics (TOG)*, 41(4):113:1–113:15, 2022.

[41] Jean-Christophe Nave, Rodolfo Ruben Rosales, and Benjamin Seibold. A gradient-augmented level set method with an optimally local, coherent advection scheme. *Journal of Computational Physics*, 229(10):3802–3827, 2010.

[42] Jean-Christophe Nave, Rodolfo Ruben Rosales, and Benjamin Seibold. A gradient-augmented level set method with an optimally local, coherent advection scheme. *Journal of Computational Physics*, 229(10):3802–3827, 2010.

[43] Stanley Osher and Ronald Fedkiw. *Level set methods and dynamic implicit surfaces*. Springer, 2003.

[44] Stanley Osher and Ronald P Fedkiw. Level set methods: an overview and some recent results. *Journal of Computational Physics*, 169(2):463–502, 2001.

- [45] Stanley Osher and James A Sethian. Fronts propagating with curvature-dependent speed: Algorithms based on hamilton-jacobi formulations. *Journal of computational physics*, 79(1):12–49, 1988.
- [46] Stanley Osher, Ronald Fedkiw, Stanley Osher, and Ronald Fedkiw. Particle level set method. *Level Set Methods and Dynamic Implicit Surfaces*, pages 79–86, 2003.
- [47] Danping Peng, Barry Merriman, Stanley Osher, Hongkai Zhao, and Myungjoo Kang. A pde-based fast local level set method. *Journal of computational physics*, 155(2):410–438, 1999.
- [48] Andrew Selle, Ronald Fedkiw, Byungmoon Kim, Yingjie Liu, and Jarek Rossignac. An unconditionally stable maccormack method. *Journal of Scientific Computing*, 35:350–371, 2008.
- [49] James A Sethian. A fast marching level set method for monotonically advancing fronts. *proceedings of the National Academy of Sciences*, 93(4):1591–1595, 1996.
- [50] James A Sethian. *Level set methods and fast marching methods*. Cambridge University Press, 1999.
- [51] James A Sethian and Peter Smereka. Level set methods for fluid interfaces. *Annual Review of Fluid Mechanics*, 35(1):341–372, 2003.
- [52] Seungwon Shin and Damir Juric. Modeling three-dimensional multiphase flow using a level contour reconstruction method for front tracking without connectivity. *Journal of Computational Physics*, 180(2):427–470, 2002.
- [53] Seungwon Shin, SI Abdel-Khalik, Virginie Daru, and Damir Juric. Accurate representation of surface tension using the level contour reconstruction method. *Journal of Computational Physics*, 203(2):493–516, 2005.
- [54] Chi-Wang Shu and Stanley Osher. Efficient implementation of essentially non-oscillatory shock-capturing schemes. *Journal of computational physics*, 77(2):439–471, 1988.
- [55] Peter Smereka. Semi-implicit level set methods for curvature and surface diffusion motion. *Journal of Scientific Computing*, 19:439–456, 2003.
- [56] Jos Stam. Stable fluids. In *Proceedings of the 26th annual conference on Computer graphics and interactive techniques*, pages 121–128, 1999.

[57] Jos Stam. Stable fluids. *ACM SIGGRAPH 99*, 1999, 11 2001. doi: 10.1145/311535.311548.

[58] Mark Sussman and Elbridge Gerry Puckett. A coupled level set and volume-of-fluid method for computing 3d and axisymmetric incompressible two-phase flows. *Journal of computational physics*, 162(2):301–337, 2000.

[59] Mark Sussman, Peter Smereka, and Stanley Osher. A level set approach for computing solutions to incompressible two-phase flow. *Journal of Computational Physics*, 114(1):146–159, 1994.

[60] Mark Sussman, Emad Fatemi, Peter Smereka, and Stanley Osher. An improved level set method for incompressible two-phase flows. *Computers & Fluids*, 27 (5-6):663–680, 1998.

[61] Tetsuya Takahashi and Christopher Batty. Fast marching-cubes-style volume evaluation for level set surfaces. 2022.

[62] Seth Taylor and Jean-Christophe Nave. A projection-based characteristic mapping method for tracer transport on the sphere. *Journal of Computational Physics*, 477:111905, 2023.

[63] Jerry Tessendorf and Brandon Pelfrey. The characteristic map for fast and efficient vfx fluid simulations. In *Computer Graphics International Workshop on VFX, Computer Animation, and Stereo Movies. Ottawa, Canada*, 2011.

[64] Grétar Tryggvason, Bernard Bunner, Asghar Esmaeeli, Damir Juric, N Al-Rawahi, W Tauber, J Han, S Nas, and Y-J Jan. A front-tracking method for the computations of multiphase flow. *Journal of Computational Physics*, 169(2):708–759, 2001.

[65] Magnus Vartdal and Arne Bøckmann. An oriented particle level set method based on surface coordinates. *Journal of computational physics*, 251:237–250, 2013.

[66] Mengdi Wang, Fan Feng, Junlin Li, and Bo Zhu. Cirrus: Adaptive hybrid particle-grid flow maps on gpu. *ACM Transactions on Graphics (TOG)*, 44(4): 1–17, 2025.

[67] Sinan Wang, Yitong Deng, Molin Deng, Hong-Xing Yu, Junwei Zhou, Duowen Chen, Taku Komura, Jiajun Wu, and Bo Zhu. An eulerian vortex method on flow maps. *ACM Transactions on Graphics (TOG)*, 43(6):1–14, 2024.

- [68] Sinan Wang, Junwei Zhou, Fan Feng, Zhiqi Li, Yuchen Sun, Duowen Chen, Greg Turk, and Bo Zhu. Fluid simulation on vortex particle flow maps. *arXiv preprint arXiv:2505.21946*, 2025.
- [69] Xi-Yuan Yin, Linan Chen, and Jean-Christophe Nave. A diffusion-driven characteristic mapping method for particle management. *SIAM Journal on Scientific Computing*, 43(5):A3155–A3183, 2021.
- [70] Xi-Yuan Yin, Olivier Mercier, Badal Yadav, Kai Schneider, and Jean-Christophe Nave. A characteristic mapping method for the two-dimensional incompressible euler equations. *Journal of Computational Physics*, 424:109781, 2021.
- [71] Xi-Yuan Yin, Kai Schneider, and Jean-Christophe Nave. A characteristic mapping method for the three-dimensional incompressible euler equations. *Journal of Computational Physics*, 477:111876, 2023.
- [72] Steven T Zalesak. Fully multidimensional flux-corrected transport algorithms for fluids. *Journal of computational physics*, 31(3):335–362, 1979.
- [73] Lanhao Zhao, Hongyan Khuc, Jia Mao, Xunnan Liu, and Eldad Avital. One-layer particle level set method. *Computers & Fluids*, 170:141–156, 2018.
- [74] Lanhao Zhao, Kailong Mu, Jia Mao, Khuc Hongyan, and Peng Dawei. A three-dimensional one-layer particle level set method. *International Journal of Numerical Methods for Heat & Fluid Flow*, 30(7):3653–3684, 2020.
- [75] Junwei Zhou, Duowen Chen, Molin Deng, Yitong Deng, Yuchen Sun, Sinan Wang, Shiying Xiong, and Bo Zhu. Eulerian-lagrangian fluid simulation on particle flow maps. *ACM Transactions on Graphics (TOG)*, 43(4):1–20, 2024.